Photon sources and their applications in quantum science and technologies

Urbasi Sinha*, Saumya Ranjan Behera, and Mehak Layal

Light and Matter Physics group, Raman Research Institute, Bengaluru, Karnataka, India
*Corresponding author: e-mail address: usinha@rri.res.in

Contents

Abstract

Single and entangled photons are ubiquitous workhorses for several quantum science and technology applications. Moreover, a photonic platform is a natural choice for testing foundational aspects of quantum mechanics. Most seminal experiments in quantum mechanics, including the work that led to the 2022 Nobel prize in Physics, have been done using photons (Aspect, Grangier, & Roger, 1981, 1982; Bouwmeester et al., 1997; Clauser & Shimony, 1978; Freedman & Clauser, 1972; Giustina et al., 2015, 2017). How do we create single photons or, for that matter, entangled photons? A large part of this chapter will be devoted to discussing the means to generate single photons. We will

see that there are two broad generation schemes: probabilistic and deterministic. In the former, one cannot deterministically generate single photons on demand, while the latter lends itself to such possibilities. We will specifically discuss spontaneous parametric downconversion (SPDC) and four wave mixing (FWM) as examples of probabilistic photon generation and quantum dots (QD) as well as color centers in diamond, including nitrogen-vacancy (NV) centers, as examples of deterministic photon generation. We will study in detail the various properties that determine the quality of the photon source. In the second part of the chapter, we will discuss the usage of single and entangled photons in different quantum technology applications. We will specifically focus our attention on two major applications, i.e., Quantum Communications and Quantum Computing. Next, we go on to discuss the various properties that single photons need to satisfy.

Keywords: Single photons, Entangled photons, Quantum technologies, Spontaneous parametric downconversion, Four wave mixing, Color centers, Quantum dots, Quantum key distribution, Quantum teleportation, Quantum computing, Quantum communications

1. Properties of single photons

We will discuss different ways of single-photon generation by exploiting the nonlinearity of specific materials, electron–hole confinement in quantum dots, and lattice defects that give rise to color centers. Single-photon generation needs to be accompanied by dedicated tests of various properties that indicate the said nature of the photons. The "singleness" of any single-photon source should be verified, and one way of verifying that is performing a $g^{(2)}$ measurement (Sinha et al., 2019).

The second-order correlation function $g^{(2)}(\tau)$ requires measuring the intensity–intensity correlation using photon detectors by adding a time delay of τ between them. This helps in differentiating between the bunching and antibunching nature of the source. Bunching of photons corresponds to the simultaneous generation of more than one photon, whereas antibunching represents single-photon emission at a time.

$$g^{(2)}(\tau) = \frac{\langle I(t)I(t+\tau)\rangle}{\langle I(t)\rangle^2} \tag{1}$$

For a classical or chaotic source of light, $g^{(2)}(\tau)$ gives a value greater than 1, showing a highly bunched nature. Any coherent source of light, like a laser, produces a $g^{(2)}(\tau)$ value 1. These single-frequency sources produce a constant number of photon counts (proportional to intensity) over time, making the time average of intensity at time 0 and τ equal. On the contrary, single-photon sources have a completely discrete nature of photon emission and

show antibunching. $g^{(2)}(0)$ indicates how likely it is to have two–photon detection from the same source of light at zero time delay between the photon detectors. For an ideal single–photon source, $g^{(2)}(0)$ becomes zero. Much effort is being made toward achieving an ideal single–photon source but only a positive $g^{(2)}$ value close to zero has been achieved for existing sources.

Fig. 1 shows a simple optical setup for measuring the second–order correlation function. A single photon is an indivisible entity. Upon incidence on one of the input ports of a 50:50 beamsplitter, it will either be transmitted or reflected with equal probability. Having a photodetector at both output ports of the beamsplitter, the cross–correlation function can be measured between the detector outputs. With a stream of single–photon inputs and zero time delay between the two detectors, we cannot have a coincidence detection, thus resulting in a zero value for $g^{(2)}(0)$. This is a signature of a true single–photon source. We get higher values for the correlation function as a function of increasing time delay. The expected dip at zero time delay for such a source is also shown in Fig. 1.

While the second–order correlation function, $g^{(2)}$, captures the single–photon character of any source, two–photon interference or the Hong–Ou–Mandel (HOM) effect can be used as a characterization tool for testing the indistinguishability of two photons (Hong, Ou, & Mandel, 1987). This is a remarkable quantum interference effect that helps characterize temporal, spatial, and spectral characters of photon pairs generated spontaneously.

In the HOM effect, two completely indistinguishable photons are incident on the input ports of a 50:50 beamsplitter, and one always measures a two–photon state at any of the output ports of the beamsplitter. When a single photon is incident on a 50:50 beamsplitter, it either gets transmitted or reflected with equal probability. Considering two indistinguishable photons at both the input ports (a,b) of a 50:50 beamsplitter, the input Fock state will
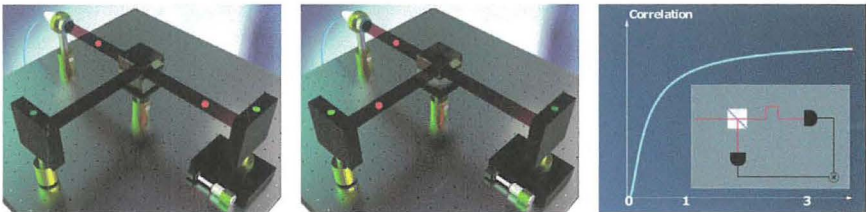

Fig. 1 Experimental schematic for $g^{(2)}$ measurement. It is also known as one–photon interference. *Adapted with permission from Sinha, U., Sahoo, S. N., Singh, A., Joarder, K., Chatterjee, R., & Chakraborti, S. (2019). Single-photon sources. Optics and Photonics News, 30(9), 32–39. https://doi.org/10.1364/OPN.30.9.000032.*

be $|1, 1\rangle_{ab}$. At the output ports (c,d), the beamsplitter output will be a super-position of the possible states $|2, 0\rangle$, $|1, 1\rangle$, and $|0, 2\rangle$ and it can be written as,

$$|1, 1\rangle_{ab} \rightarrow |2, 0\rangle_{cd} + |1, 1\rangle_{cd} - |1, 1\rangle_{cd} - |0, 2\rangle_{cd} \qquad (2)$$

In Eq. (2), the first and fourth terms on the right–hand side represent the case where one input photon gets transmitted, the other gets reflected, and both exit together at the same output port of the beamsplitter. On the other hand, the middle terms represent the cases when both the photons either get trans-mitted or reflected exiting at different ports of the beamsplitter. The negative sign before the last two terms is caused by a π phase shift from reflection off the dielectric coating inside the beamsplitter, while the reflection for a pho-ton approaching the coated surface from behind does not induce a phase change. As the two incident photons are indistinguishable at zero time delay, the two terms in the middle cancel out, showing a destructive interference, and hence the equation modifies to,

$$|1, 1\rangle_{ab} \rightarrow |2, 0\rangle_{cd} - |0, 2\rangle_{cd} \qquad (3)$$

The second–order interference effect results in a two–photon emission on either of the output port. In Fig. 2, the architecture required for doing a two–photon interference is shown. With the photons being indistinguishable, one of the two detectors will click, giving zero coincidence detection (Fig. 2A). Both in Fig. 2A and B, one of the inputs can be seen mounted on a micrometer stage, which can be used to create a delay between the two input photons introducing distinguishability. This causes the two–photon probability ampli-tudes to interfere constructively and give nonzero coincidence detection between both detectors (Fig. 2B). The zero coincidence causes the dip (HOM dip) in Fig. 2C only when the delay between the arrival time of both photons is zero. With the increasing time delay, the correlation between the two detections increases, generating the entire HOM characteristic plot.
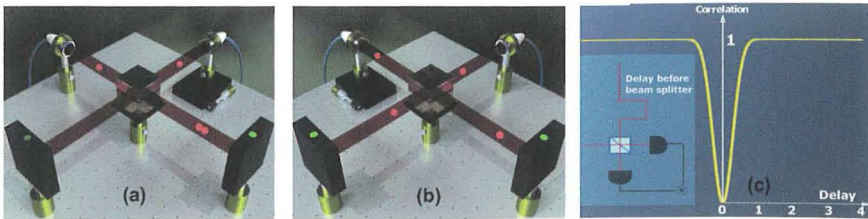

Fig. 2 Experimental representation of HOM effect, also known as two-photon interfer-ence. *Adapted with Permission from Sinha, U., Sahoo, S. N., Singh, A., Joarder, K., Chatterjee, R., & Chakraborti, S. (2019). Single-photon sources. Optics and Photonics News, 30(9), 32–39. https://doi.org/10.1364/OPN.30.9.000032.*

In this chapter, we will go through the characteristics of various types of single-photon sources, the physics behind their working principles, existing state-of-the-art technologies, and their potential applications. The next few sections focus on various probabilistic sources like SPDC and FWM. Certain nonlinear crystals, during an interaction with a strong electromagnetic field, can emit photons in a spontaneous manner, which is the working principle behind these sources.

2. Spontaneous parametric downconversion

Spontaneous parametric downconversion (SPDC) is a nonlinear optical process that occurs in certain types of nonlinear media. In SPDC, a photon spontaneously splits into two other photons of lower energies. Currently, SPDC is vastly used as a resource for quantum communications, quantum metrology, and quantum cryptographic applications. SPDC is also a common choice for entangled photon pair generation needed for various foundational and applied quantum technology studies. The photon pair generation aspect of the SPDC process proves to be very useful with the heralded usage of single photons. The presence of the other photon is signaled when one of the photons is detected. Therefore, these sources are also called heralded photon sources. Here, we focus on the physics underlying this process and highlight a few important properties of SPDC. First, we discuss the quantum nature and the physics behind the photon generation process for different types of SPDC. In the latter part, we learn more about applications of SPDC with state-of-the-art implementations of the same. This discussion aims at giving a young researcher the necessary first elements needed to work with SPDC sources of light.

Parametric downconversion in the frequency of the electric field results from a nonlinear interaction of the field with the medium. Such phenomena occur at a very high intensity of the pump radiation. The induced polarization is so strongly affected by the radiation that it deforms beyond the linear response that generates the usual dispersion and absorption. From Maxwell's equations, assuming a medium that is uniform, nonmagnetic, source-free, and with a nonlinear polarization response, the wave equation can be written as.[a]

---

[a] Vector/tensor notations are not being used for simplicity, and the same convention will be followed throughout the chapter.

$$\nabla \times \nabla \times E = \nabla(\nabla.E) - \nabla^2 E = -\mu_0 \frac{\partial^2 D}{\partial t^2} \tag{4}$$

where electric displacement field D is:

$$D = \varepsilon_0 E + P_1 + P_{NL} = D_1 + P_{NL} \tag{5}$$

where P is the electric dipole moment of the material, known as polarization density. P_{NL} is the nonlinear polarization density term, P_1 is the first-order polarization (linear in E), and D_1 is the first-order electric displacement field. Assuming that the medium is isotropic in its linear properties, we can write $D_1 = n^2 \varepsilon_0 E$, where n is the refractive index of the medium.

Further solving the wave equation,

$$\nabla^2 E - \frac{1}{c^2}\frac{\partial^2 E}{\partial t^2} = \mu_0 \frac{\partial^2 P}{\partial t^2} \tag{6}$$

As $P = P_1 + P_{NL}$ and $P_1 = \varepsilon_0 \chi^{(1)} E$,

$$\nabla^2 E - \left(\frac{1 + \chi^{(1)}}{c^2}\right)\frac{\partial^2 E}{\partial t^2} = \mu_0 \frac{\partial^2 P_{NL}}{\partial t^2} \tag{7}$$

The simplified wave equation is now given by:

$$\nabla^2 E - \frac{n^2}{c^2}\frac{\partial^2 E}{\partial t^2} = \mu_0 \frac{\partial^2 P_{NL}}{\partial t^2} \tag{8}$$

We can expand the nonlinear polarization in a power series in the applied radiation field to better understand the optical nonlinear response of any material. Highly anisotropic crystals are frequently employed in nonlinear optics, and their response is represented in the tensorial form by

$$P = \varepsilon_0 \chi_i^{(1)} E + \varepsilon_0 \chi_{ij}^{(2)} E^2 + \varepsilon_0 \chi_{ijk}^{(3)} E^3 + \cdots \tag{9}$$

$\chi^{(m)}$ is the m-th order electric susceptibility tensor (Boyd, 2020). The second term on the right-hand side of the above equation is responsible for parametric downconversion processes.

Fig. 3A shows one pump photon splitting into two photons, namely "Signal" and "Idler" photons, as a result of SPDC. Let us now look at this from a quantum mechanical point of view. A nonlinear medium, when pumped by a photon with frequency ω_p, generates an identical photon pair of frequency $\omega = \omega_p/2$. The process is known as degenerate parametric downconversion, i.e., the energy of the downconverted photons is equal and exactly half of the pump photon. Else, the process is termed
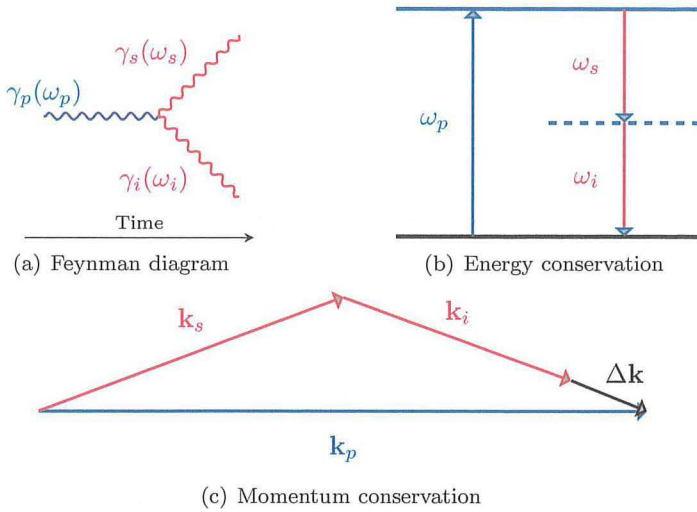
(a) Feynman diagram   (b) Energy conservation

(c) Momentum conservation

Fig. 3 (A) Feynman diagram representing noncollinear phase-matching condition. (B) One pump photon with energy $\hbar\omega_p$ splits into two photons named signal and idler with energies $\hbar\omega_s$ and $\hbar\omega_i$ respectively, and they satisfy energy conservation. (C) The momentum vectors of the pump, signal, and idler are k_p, k_s, and k_i, respectively, and they satisfy momentum conservation at phase-matching conditions. *Adapted with permission from Singh, A., (2021). Creation, characterization, and manipulation of quantum entanglement in a photonic system (Ph.D. thesis). New Delhi: Jawaharlal Nehru University.*

nondegenerate SPDC. We have the Hamiltonian for the degenerate SPDC (Gerry, Knight, & Knight, 2005) as

$$\hat{H} = \hbar\omega\hat{a}^\dagger\hat{a} + \hbar\omega_p\hat{b}^\dagger\hat{b} + i\hbar\chi^{(2)}(\hat{a}^2\hat{b}^\dagger - \hat{a}^{\dagger 2}\hat{b}) \tag{10}$$

Here, $\hat{b}$ is the pump mode, and $\hat{a}$ is the signal mode. And $\chi^{(2)}$ is the second-order nonlinear susceptibility.

For a nondegenerate case, assuming the pump field is quantized, the Hamiltonian takes the form

$$\hat{H} \approx \chi^{(2)}\hat{a}_p\hat{a}_s^\dagger\hat{a}_i^\dagger + c.c \tag{11}$$

where $\hat{a}_p$ is the annihilation operator of the pump beam and $\hat{a}_s^\dagger$ and $\hat{a}_i^\dagger$ are the creation operators for the signal and idler photons, respectively. Assuming signal and idler modes initially in vacuum states, the simultaneous generation of the pair photons will be as follows

$$|1\rangle_p|0\rangle_s|0\rangle_i \Rightarrow \hat{a}_p\hat{a}_s^\dagger\hat{a}_i^\dagger|1\rangle_p|0\rangle_s|0\rangle_i = |0\rangle_p|1\rangle_s|1\rangle_i \tag{12}$$

While the downconversion process takes place, both energy and momentum need to be conserved (Fig. 3). Hence, the following conditions need to be satisfied.

$$\hbar\omega_p = \hbar\omega_s + \hbar\omega_i \tag{13}$$

$$k_p = k_s + k_i \Rightarrow \Delta k = k_p - (k_s + k_i) \simeq 0 \tag{14}$$

where k_p, k_s, and k_i are the momentum vectors corresponding the frequencies ω_p, ω_s, and ω_i of the pump, signal, and idler photons, and ΔK is the phase mismatch term. The wave vectors have to satisfy Eq. (14) to have an efficient nonlinearity. These above two equations are called "phase-matching" conditions as shown in Fig. 3.

There are three types of SPDC processes depending on the nonlinear medium used. Type-0 SPDC is where all three waves, pump, signal, and idler share the same polarization. In type-I SPDC, the signal and idler are generated to have the same polarization but orthogonal to that of the pump polarization. In the type-II case signal and idler, polarization is orthogonal to each other.

For type-I case, the interaction Hamiltonian will be,

$$\hat{H}_I = \hbar\eta\hat{a}_s^\dagger\hat{a}_i^\dagger + c.c. \tag{15}$$

In "parametric approximation", we assume that the pump field is a strong coherent classical field, which is strong enough to remain undepleted of photons over the relevant time scale. Under this approximation, $\eta \propto \chi^{(2)}E_p$, where E_p is the amplitude of the strong coherent classical field. The photons emerge along the opposite sides of two concentric cones satisfying the phase-matching condition. Fig. 4 illustrates the experimental schematic of an in-lab realization of type-I SPDC in a noncollinear configuration. Fig. 5 shows the results of an experimental type-I SPDC realization of collinear and noncollinear configurations captured by a CMOS camera.

For the type-II SPDC, the birefringence effects of the nonlinear medium cause the signal and idler photons to be emitted along two cones as ordinary wave (o) and extraordinary wave (e) corresponding to the two orthogonal polarizations. Fig. 6 shows an experimental schematic of a type-II SPDC process. At the points where the cones intersect, the photons will be indistinguishable in the sense that it is not possible to determine from which cone a photon is obtained. So, by screening the other parts of the cones and putting pinholes at the intersection of the two cones, we can get polarization-entangled photon pairs through the aperture (Fig. 7).
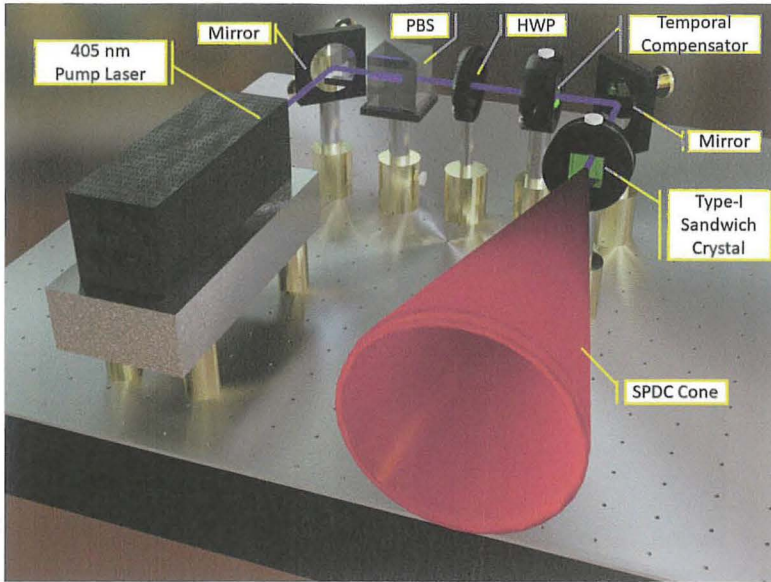
Fig. 4 Schematic of a type-I SPDC (noncollinear) process resulting in concentric cones where the pair of photons collected from diametrically opposite sides of the ring are entangled in polarization degree of freedom. *Adapted with permission from Singh, A., (2021). Creation, characterization, and manipulation of quantum entanglement in a photonic system (Ph.D. thesis). New Delhi: Jawaharlal Nehru University.*

Fig. 5 Type-I SPDC ring in collinear (*left*) and noncollinear (*right*) configurations imaged by a CMOS camera. *Adapted with Permission from Singh, A., (2021). Creation, characterization, and manipulation of quantum entanglement in a photonic system (Ph.D. thesis). New Delhi: Jawaharlal Nehru University.*

Considering the photons are either horizontally or vertically polarized, the interaction Hamiltonian for type–II SPDC can be written as

$$\hat{H}_{II} = \hbar\eta(\hat{a}^\dagger_{Vs}\hat{a}^\dagger_{Hi} + \hat{a}^\dagger_{Hs}\hat{a}^\dagger_{Vi}) + c.c. \tag{16}$$

Using the Hamiltonian, we can define the state evolution of the photon pair in time, and we have

Fig. 6 Schematic of type-II SPDC (noncollinear) process resulting in intersecting cones where the photons on intersection points are entangled in polarization degree of freedom. *Adapted with Permission from Singh, A., (2021). Creation, characterization, and manipulation of quantum entanglement in a photonic system (Ph.D. thesis). New Delhi: Jawaharlal Nehru University.*
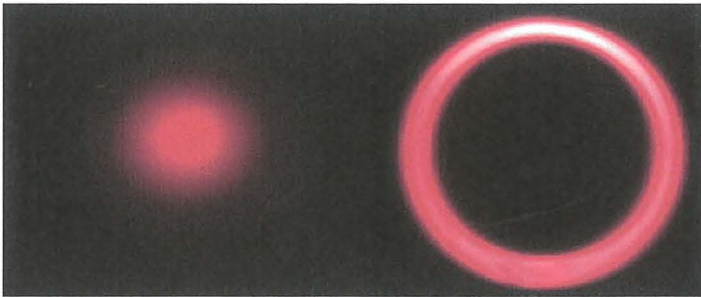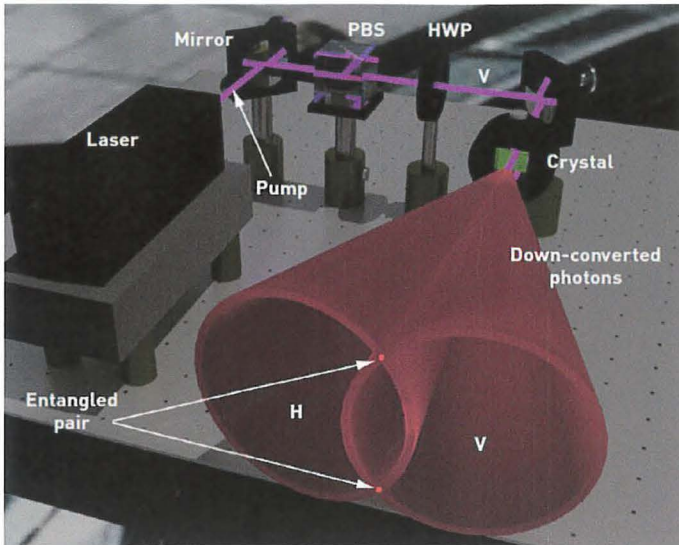

Fig. 7 Type-II SPDC rings in collinear (*left*) and noncollinear (*right*) configurations imaged by a CMOS camera. In the overlapping region of the two rings, indistinguishability comes into play as one cannot comment on which ring the photon belongs to. Thus, a pair of photons collected from these regions will be entangled in polarization degrees of freedom. *Adapted with permission from Singh, A., (2021). Creation, characterization, and manipulation of quantum entanglement in a photonic system (Ph.D. thesis). New Delhi: Jawaharlal Nehru University.*
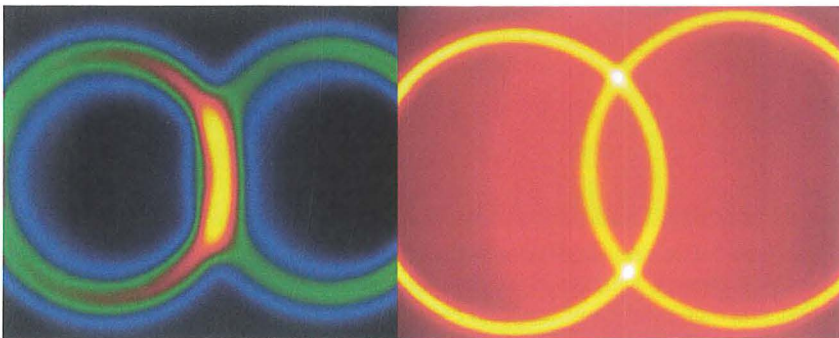
$$|\psi(t)\rangle = \exp(-it\hat{H}_{II}/\hbar)|\psi_0\rangle \tag{17}$$

With the Hamiltonian having no explicit time dependence, the evolution operator can be expanded.

$$|\psi(t)\rangle \approx 1 - it\hat{H}_{II}/\hbar + \frac{1}{2}\left(-it\hat{H}_{II}/\hbar\right)^2|\psi_0\rangle \tag{18}$$

For type-0 and type-I SPDC, the photon pair mode is initially in a vacuum state, i.e., $|\psi_0\rangle = |0\rangle_s|0\rangle_i$. So, we write the evolved state as

$$|\psi(t)\rangle = |0\rangle_s|0\rangle_i - \frac{\mu^2}{2}|2\rangle_s|2\rangle_i - i\mu|1\rangle_s|1\rangle_i \tag{19}$$

where $\mu = \eta t$. The state vector can be normalized, and we can drop the μ^2 term containing $|2\rangle_s|2\rangle_i$ state.

For type-II SPDC, an initial mode for the photon pair in a vacuum state is given as

$$|\psi_0\rangle = |0\rangle_{Vs}|0\rangle_{Hs}|0\rangle_{Vi}|0\rangle_{Hi} \tag{20}$$

$$|\psi(t)\rangle = -i\mu\frac{1}{\sqrt{2}}[|1\rangle_{Vs}|0\rangle_{Hs}|0\rangle_{Vi}|1\rangle_{Hi} + |0\rangle_{Vs}|1\rangle_{Hs}|1\rangle_{Vi}|0\rangle_{Hi}] \tag{21}$$

After dropping the vacuum states and higher orders of μ, we are left with the above evolved normalized photon pair state from the type-II SPDC process.

$$|\psi(t)\rangle = -i\frac{\mu}{\sqrt{2}}[|V\rangle_s|H\rangle_i + |H\rangle_s|V\rangle_i] \tag{22}$$

By normalizing the state in Eq. (22), we will obtain one of the four maximally entangled Bell states.

Phase-matching conditions for SPDC are only satisfied in certain non-centrosymmetric crystals like *BBO*, *KD$_2$PO$_4$*, *KDP*, *PPLN*, and *PPKTP*, which have nonvanishing $\chi^{(2)}$ value. When $\Delta K = 0$, phase matching is accomplished. Collinear phase matching occurs when the K vectors of the pump, signal, and idler are parallel. When K vectors of all involved photons are not parallel, we can get noncollinear phase matching. Phase matching can be accomplished by either the quasi–phase-matching (QPM) or the critical (birefringent) phase-matching method. By periodically inverting the sign of second-order nonlinearity $\chi^{(2)}$ throughout the crystal's length, quasi–phase matching (QPM) is accomplished. Downconverted photons originating in the inverted portion of the crystal are 180 degrees out of phase with the photons created from the same point when the crystal is not poled. One can expect a partial constructive interference of newly generated photons with

those created in previous locations in the crystal by carefully selecting the pol-
ing period for flipping the crystal orientation. High conversion efficiency is
achieved due to the growth in the number of downconverted photons as
the pump beam moves through the periodically poled crystal. Birefringent
phase matching corrects for the material dispersion by making use of the
medium's birefringence and can be interpreted as the intersection point of
the ordinary and extraordinary refractive index surface diagrams at fundamen-
tal and downconverted frequencies corresponding to the nature of the crystal
and type of the SPDC process required (Couteau, 2018). Also, by suitably
choosing the poling period, type-0 QPM with all three fields with the same
polarization can be achieved in addition to type-I and type-II QPM.

2.1 Entangled photon sources

Entanglement is the quantum correlation, which is frequently employed in
various quantum technologies. As a result, the creation of entangled photons
becomes very important for many applications. The nonlinear optical pro-
cess of SPDC in type-II, two crystal geometry in type-I SPDC, as well as in
type-0 SPDC results in high-quality polarization-entangled photons. In one
of the type-I SPDC approaches, the two identical BBO crystals are oriented
so that the horizontal (or vertical) plane is defined by the first (or second)
crystal's optic axis and pump beam propagation direction, respectively
(Singh, 2021). Imagine such a crystal is incident with a horizontally (verti-
cally) polarized pump beam. In that situation, downconversion will take
place in the first (second) crystal, where type-I coupling has caused the pump
beam to be extraordinarily polarized. As a result, vertically (or horizontally)
polarized photons from the first (or second) crystal are produced as down-
converted light cones. A diagonally polarized pump beam has an equal
chance of down-converting from either the first or the second crystal under
no pump depletion approximation, and if the spatial overlap of the two
downconversion cones is sufficient, the two polarization amplitudes add
coherently to produce a state given by

$$|\Psi\rangle = (|HH\rangle + e^{(i\phi)}|VV\rangle)/\sqrt{2} \tag{23}$$

The spatial overlap of the light cones is defined by the parameter $\theta_{dc}L/D$,
where θ_{dc} is the cone opening angle, L is the crystal thickness, and D is
the pump beam diameter. For coherent addition of the downconverted
polarization amplitudes from the two crystals, we must have $\theta_{dc}L/D \gg 1$.
In Fig. 8, the schematic for the generation of the entangled state, discussed
in Eq. (23), using a type-I sandwiched nonlinear crystal geometry, is shown.
As illustrated in the figure, one can measure the entangled state produced by
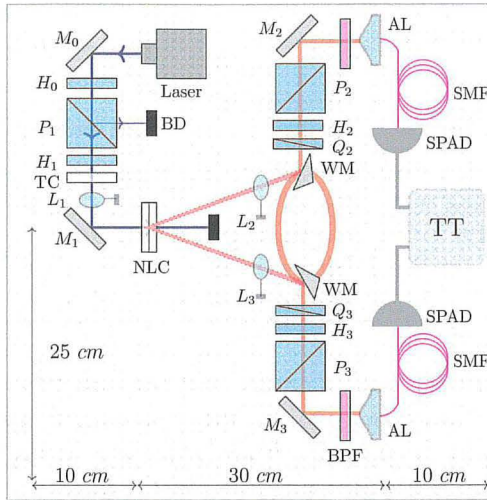
Fig. 8 Diagram of the experimental setup used to establish an SPDC-based type-I polarization-entangled photon source utilizing a BBO crystal in a two-crystal (sandwich) architecture and characterize it using quantum state tomography. Nomenclature for symbols: *P*, polarizing beamsplitter; *Q*, quarter-wave plate, *H*, half-wave plate; *NLC*, nonlinear crystal; *TC*, temporal compensator; *L*, plano-convex lens; *M*, mirror; *WM*, wedge mirror; *BPF*, bandpass filter; *AL*, aspheric lens; *SMF*, single-mode fiber; *SPAD*, single-photon avalanche diode; and *TT*, time tagger unit or coincidence module. *Adapted with permission from Singh, A., (2021). Creation, characterisation, and manipulation of quantum entanglement in a photonic system (Ph.D. thesis). New Delhi: Jawaharlal Nehru University.*

Table 1 State of the art for SPDC-based photon sources with reference to the nature of the source, emission range, bandwidth, operating temperature, emission direction, and efficiency.

Probabilistic/ deterministic	Emission range	Bandwidth	Operating temperature	Emission direction	Efficiency
Probabilistic	600–1700 nm	nm	243–473 K	Narrow	0.84 (Pereira et al., 2013)

doing quantum state tomography using a combination of a quarter–wave plate, a half–wave plate, and a polarizing beamsplitter.

Periodically poled crystals, especially PPKTP, are being used in a polarization–based Sagnac interferometer to generate Type–0 and Type–II entangled photons. PPKTP crystals are quasi–phase–matched at a particular temperature for different wavelengths of signal and idler. Hence, the wavelengths of the entangled photons can be modulated easily by changing the temperature of the oven in which the crystal is kept. Tables 1 and 2 show the

Table 2 State of the art for SPDC-based photon sources concerning brightness, $g^{(2)}$, entanglement fidelity, HOM visibility, and applications in quantum science and technologies.

Brightness	Best $g^{(2)}$	Entanglement fidelity	HOM visibility	Quantum applications
1 MHz/mW (Cao et al., 2018)	0.004 (Massa et al., 2019)	0.9959 (Fedrizzi, Herbst, Poppe, Jennewein, & Zeilinger, 2007)	0.995 (Lee, Kim, & Lee, 2021)	Metrology, information processing, foundations, and communications

state of the art for SPDC-based photon sources with reference to the nature of the source, emission range, bandwidth, operating temperature, emission direction, efficiency, brightness, $g^{(2)}$, entanglement fidelity, HOM visibility, and applications in quantum science and technologies.

- The 1 MHz/mW brightness reported in Table 2 is the observed generation rate per mW of pump power   (Cao et al., 2018).
- For waveguide-based SPDC, a $g^{(2)}$ value of 0.022 ± 0.004 and HOM visibility of 0.995 ± 0.018 has been observed. This source had a brightness of 45 MHz/mW (Zhao, Ma, Rüsing, & Mookherjea, 2020).

3. Four-wave mixing

Nonlinear optical media with isotropic or centrosymmetric structure have a near-zero second-order nonlinear optical susceptibility $\chi^{(2)}$ and hence, a relatively high value for the third-order susceptibility $\chi^{(3)}$. In such nonlinear crystals, processes like spontaneous parametric downconversion or Second Harmonic generation which require $\chi^{(2)}$ susceptibility are impossible. Instead, processes which describe the interaction of four waves to produce new frequencies during the propagation through the medium due to the presence of $\chi^{(3)}$ susceptibility are more likely to take place. Third Harmonic generation, four-wave mixing (FWM)-like effects are governed by dominant third-order nonlinearity $\chi^{(3)}$ in the medium as shown in Fig. 9. We will focus on the four-wave mixing phenomenon in this section and discuss the single-photon generation using the same.

Four-wave mixing is a process where two pump photons annihilate themselves, generating sidebands spaced at equal frequency intervals from the pump and are called Stokes and anti-Stokes photons. This will occur provided the total momentum and energy are conserved

$$2K_p = K_s + K_i \Rightarrow \Delta K = 2K_p - K_s - K_i \simeq 0 \qquad (24)$$
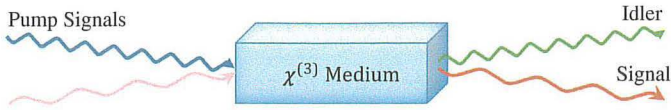
Fig. 9 Generation of Signal and Idler photons by pumping of a $\chi^{(3)}$ medium (Four-Wave Mixing Schematics).
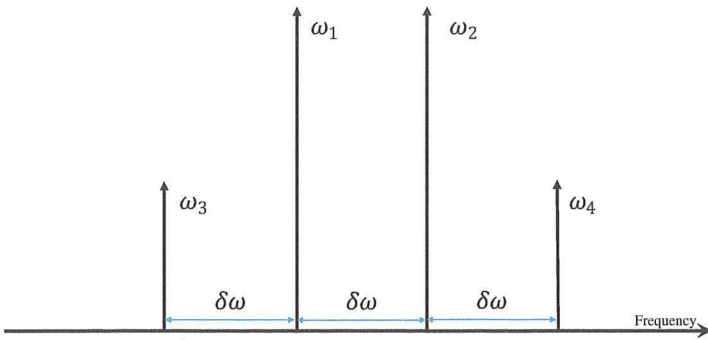

Fig. 10 Degenerate Four-Wave mixing: Stokes and anti-stokes lines formation with pump ω_1 and ω_2 separated by $\delta\omega$ frequency.

$$2\omega_p = \omega_s + \omega_i \qquad (25)$$

where K_p, K_s, and K_i are the wavevectors and ω_p, ω_s, and ω_i are the frequencies corresponding to pump, signal, and idler modes, respectively.

Let us assume one case of FWM, where two different copropagating frequencies ω_1 and ω_2 ($\omega_2 > \omega_1$) separated by $\delta\omega$ frequency being given as inputs to the system.

By the refractive index modulation, FWM will generate two new frequencies ω_3 and ω_4 such that

$$\omega_3 = 2\omega_1 - \omega_2 = \omega_1 - \delta\omega \qquad (26)$$
$$\omega_4 = 2\omega_2 - \omega_1 = \omega_2 + \delta\omega \qquad (27)$$

This third-order nonlinear process of using two different waves at a certain frequency gap as inputs and producing the outputs at the same frequency gaps from the input frequencies is called degenerate FWM (Fig. 10), where ω_1 or ω_2 is used twice to generate the other two frequencies. The nonlinear polarization component here can be defined as

$$P_{NL} = \varepsilon_0 \chi^{(3)} [E(\omega_1) + E(\omega_2) + c.c]^3 \qquad (28)$$

During FWM process, with preexisting ω_1 and ω_2 in the system frequency ω_3 or ω_4 can be amplified, i.e., the frequency components experience parametric amplification.

A more general case will be when three different frequencies combine as a result of third–order nonlinearity and give rise to the resultant frequency

$$\omega_4 = \pm\omega_1 \pm \omega_2 \pm \omega_3 \qquad (29)$$

where $\omega_1 \neq \omega_2 \neq \omega_3$.

This is known as a nondegenerate four-wave mixing process (Fig. 11). There are eight different ways that the waves can combine, producing different frequencies. P_{NL} for such a process involving three distinct waves will be

$$P_{NL} = \varepsilon_0 \chi^{(3)} [E(\omega_1) + E(\omega_2) + E(\omega_3) + c.c]^3 \qquad (30)$$

Degenerate FWM is a special case of nondegenerate FWM, where two of the four frequencies coincide.

Let us assume the case where $\omega_4 = \omega_1 + \omega_2 + \omega_3$. Here, the generation of frequency ω_4 is governed by the nonlinear wave equation
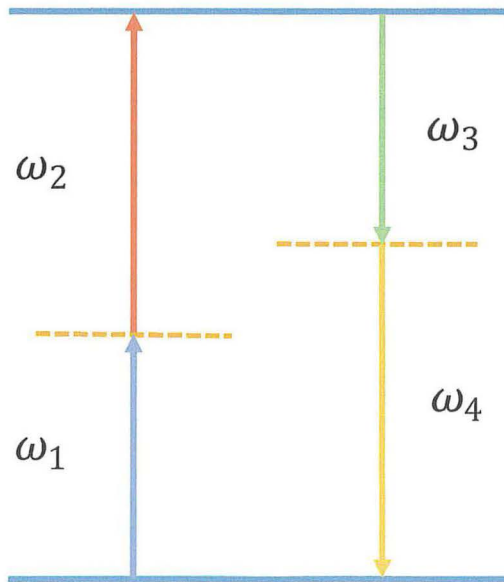

Fig. 11 Nondegenerate Four-Wave interaction where ω_4 is generated by a certain combination of other three frequencies.

$$\nabla^2 E(\omega_4) - \mu_0 \varepsilon n^2 \frac{\partial^2 E(\omega_4)}{\partial t^2} = \mu_0 \frac{\partial^2 P_{NL}^{(4)}}{\partial t^2} \tag{31}$$

The term on the right-hand side of Eq. (8) is the nonlinear source term. To figure out how the incident beams propagate through the nonlinear medium, we assume $E(\omega_4) = \frac{1}{2}[E_4 e^{-i\omega_4 t} + c.c.] = \frac{1}{2}[A_4 e^{i(k_4 z - \omega_4 t)} + c.c.]$, where A_4 is the slowly varying amplitude corresponding to the field associated to frequency ω_4, i.e., the longitudinal variation of the amplitude occurs over much larger distances than the optical wavelength (Agrawal, 2013). We can solve the above equation by substituting $E(\omega_4)$. We will get the first term in the equation as

$$\nabla^2 E(\omega_4) = \left(\frac{\partial^2}{\partial x^2} + \frac{\partial^2}{\partial y^2} + \frac{\partial^2}{\partial z^2} \right) A_4 e^{i(k_4 z - \omega_4 t)} \tag{32}$$

$$\nabla^2 E(\omega_4) = \left[\frac{\partial^2 A_4}{\partial z^2} - 2ik_4 \frac{\partial A_4}{\partial z} - A_4 k_4^2 \right] e^{i(k_4 z - \omega_4 t)} \tag{33}$$

From the slowly varying amplitude approximation, $|\frac{\partial^2 A_4}{\partial z^2}| \ll |2ik_4 \frac{\partial A_4}{\partial z}|$.
    The second term also can be calculated as

$$\mu_0 \varepsilon \frac{\partial^2 E(\omega_4)}{\partial t^2} = -\frac{n^2 \omega_4^2}{c^2} A_4 e^{i(k_4 z - \omega_4 t)} = -k_4^2 A_4 e^{i(k_4 z - \omega_4 t)} \tag{34}$$

Substituting the above expression, we can rewrite Eq. (8) as

$$-2ik_4 \frac{\partial A_4}{\partial z} e^{i(k_4 z - \omega_4 t)} = \mu_0 \frac{\partial^2 P_{NL}^{(4)}}{\partial t^2} \tag{35}$$

We can write the nonlinear polarization term with frequency ω_4 from Eq. (7) as

$$P_{NL}^{(4)} = \frac{3}{2} \varepsilon_0 \chi^{(3)} A_1 A_2 A_3 e^{i((k_1 + k_2 + k_3)z - \omega_4 t)} \tag{36}$$

Here, in the expression for nonlinear polarization $P_{NL}^{(4)}$, we are only considering the terms giving rise to the frequency ω_4 and not the self-phase modulation or the cross-phase modulation terms.

$$-2ik_4 \frac{\partial A_4}{\partial z} e^{i(k_4 z - \omega_4 t)} = \frac{3}{2} \mu_0 \varepsilon_0 \omega_4^2 \chi^{(3)} A_1 A_2 A_3 e^{i((k_1 + k_2 + k_3)z - \omega_4 t)} \tag{37}$$

$$\frac{\partial A_4}{\partial z} = \frac{3i\omega_4^2}{4k_4 c^2} \chi^{(3)} A_1 A_2 A_3 e^{i\Delta k z} \tag{38}$$

where $\Delta k = k_1 + k_2 + k_3 - k_4$. Satisfying the phase-matching condition, i.e., $\Delta k = 0$, will make FWM happen with maximum efficiency. Eq. (15) is the
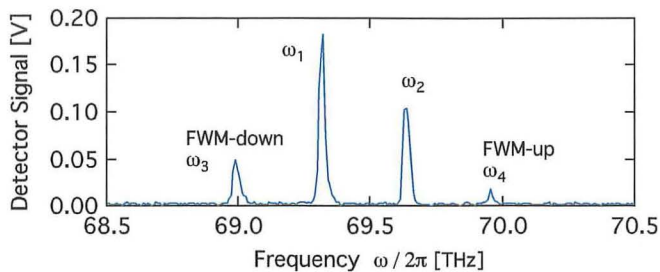
Fig. 12 Experimentally measured spectrum of the FWM with frequency difference between pump sources ω_1 and ω_2 with $\delta\omega = 2\pi \times 314GHz$. ω_3 and ω_4 peaks are generated at the locations expected by energy conservation from degenerate FWM. Pump frequencies are measured with additional optical attenuators to protect the detectors. *Adapted with permission from Friedli, P., Sigg, H., Hinkov, B., Hugi, A., Riedi, S., Beck, M., & Faist, J. (2013). Four-wave mixing in a quantum cascade laser amplifier. Applied Physics Letters, 102(22), 222104. https://doi.org/10.1063/1.4807662.*

coupled wave equation that describes the propagation of the field associated with ω_4 inside the nonlinear media. The above description can also be understood as a sum frequency generation where three different frequencies give rise to a much higher frequency field. FWM also involves difference frequency generation where the output frequency is the sum of two frequencies minus the third frequency (Fig. 12; Friedli et al., 2013).

Four-wave mixing in fibers is related to self-phase modulation and cross-phase modulation originating from Kerr nonlinearity. In fiber WDM (wavelength division multiplexing) systems, four-wave mixing can cause cross talks between different frequency components affecting optical fiber communication. The efficiency of the four-wave mixing process can be reduced by introducing nonzero dispersion-shifted fibers causing the reduction in intermodulation of input signals. But, also, in WDM channels, four-wave mixing is employed in a controlled manner to get desired optical frequency at the output.

Four-wave mixing is very promising in the case of single-photon generation. Degenerate four-wave mixing can be used to produce correlated photon pairs, i.e., entangled photon pairs. When compared to SPDC-based sources, waveguide-based sources that employ the four-wave mixing principle have a higher pair production rate. According to Fiorentino et al. (2007), these sources have a high measured coincidence of single photon pairs per second per mW of pump power, which is about 50 times greater than the bulk SPDC. This is because fewer spatial modes interact with waveguides, whereas a bulk crystal's pump mode interacts with the continuum of spatial modes. Additionally, whereas the spectral density in bulk crystals is linearly dependent on the crystal's size, it depends

Table 3 State of the art for FWM-based photon sources with reference to nature of the source, emission range, bandwidth, operating temperature, emission direction, and efficiency.

| Probabilistic/ deterministic	Emission range	Bandwidth	Operating temperature	Emission direction	Efficiency
Probabilistic	600–1550 nm	10 nm	Room temperature	Narrow	0.26 (Smith, Mahou, Cohen, Lundeen, & Walmsley, 2009)

Table 4 State of the art for FWM-based photon sources with reference to brightness, $g^{(2)}$, entanglement fidelity, HOM visibility, and applications in quantum science and technologies.

Brightness	Best $g^{(2)}$	Entanglement fidelity	HOM visibility	Quantum applications
2×10^{11} Hz (Steiner et al., 2021)	0.003 (Petrov, Fedotov, & Zheltikov, 2019)	0.997 (Massa et al., 2019)	0.97 (Jiang, Lu, Zhang, Painter, & Lin, 2015)	Integrated photonics

quadratically on the length of waveguides. Tables 3 and 4 show various cutting-edge parameters for photon sources based on FWM.

- In Table 4, Brightness = (pair generation rate per pump power square)/ (emission spectral width of FWHM).

In the next two sections, we will discuss in detail the deterministic sources like quantum dots and color centers of light where controlled excitation of atoms or atom-like systems can lead to the on-demand emission of single photons.
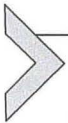
4. Quantum dot sources

Single-photon emitting sources can be much more enabling in many quantum communication or quantum information processing-based applications when the emission is deterministic. In the domain of deterministic coherent single-photon sources, the use of two-level systems based on quantum dots is emerging and laying down a very promising architecture. Quantum dots are zero-dimensional particles of semiconductor materials with a diameter of 2–10 nm with distinct electrical and optical properties that lie somewhere between that of the bulk semiconductors and individual atoms or molecules, which can be attributed to their small size and high surface-to-volume ratio. A quantum dot being a single emitter can be counted as one photon source. With a definite number of nanocrystals (quantum

dots), we can control the number of single photons produced. In a bulk semiconductor, repulsive Coulombic potential and Pauli's exclusion principle forbid the electrons from entering the neighboring atom orbitals already occupied by the core electrons. Thus, the interaction potential between neighboring atoms in a lattice is weak. It can also be referred to as a perturbation potential applied to free electrons. The solutions to this Schrödinger's equation are represented by Bloch functions which are nothing but the modified forms of plane waves in the presence of this weak potential (Ashcroft & Mermin, 2022).

$$\psi_k(r) = \sum_k c_{k-K} \exp^{i(k-K).r} \tag{39}$$

where k is crystal momentum and K is general reciprocal lattice vectors for the crystal. The coefficients c_{k-K} and energy of the level E are given by the Schrödinger equation where $U_{K'-K}$ is the weak potential.

$$\left[\frac{\hbar^2}{2m}(k-K)^2 - E\right]c_{k-K} + \sum_{K'} U_{K'-K}c_{k-K'} = 0 \tag{40}$$

Due to the wave function overlap of the neighboring atoms, intermixing of the valence shell electrons takes place, which gives rise to many closely placed energy levels that look like a continuous energy band. Since quantum dots are crystals of nanometer scale, there are only hundreds of atoms in each crystal. Due to a balance between the reduced numbers and ultrafine size, most of the electrons are bound to their valence shells resulting in the discretization of otherwise delocalized energy states.

4.1 Quantum confinement

The spatial confinement of electron–hole pairs (excitons) in one or more dimensions within a semiconductor material is known as the quantum confinement effect. Even though discrete energy levels arise as a result of a low number of atoms, the quantum confinement effect is observed when the size of the crystal approaches the de Broglie wavelength of the electron or double the Bohr radius of excitons. It is more prominent in semiconductors than metals because of comparatively larger energy band gaps in the electronic band structures. The quantum confinement effect can further be classified into three categories based on the degree of spatial confinement of the excitons. In a bulk semiconductor material, the electrons transitioned to the conduction band are not constrained to move in any particular direction. When the electrons or excitons are confined in one spatial dimension, the energy

levels are confined in a 2D potential well, otherwise called a quantum well. Similarly, excitons confined in two spatial dimensions give rise to the quantum wire, a suitable analog for which is a 1D quantum box and excitons confined in all three spatial dimensions are called quantum dots with the corresponding potential structure in 0D (Ramalingam et al., 2020).

Due to tightly confined electron–hole pairs in the energy bands, respective energy levels act as two quantized energy levels of individual atoms. For possessing such atom-like features, quantum dots are also referred to as artificial atoms. As we go toward a smaller quantum dot, fewer atoms are present in a crystal which leads to fewer interactions and smaller widths of the energy bands, thereby increasing the gap between the conduction and valence bands as shown in Fig. 13. Hence, the emission wavelength can be modulated by band gap tuning, a consequence of a change in the shape, size,
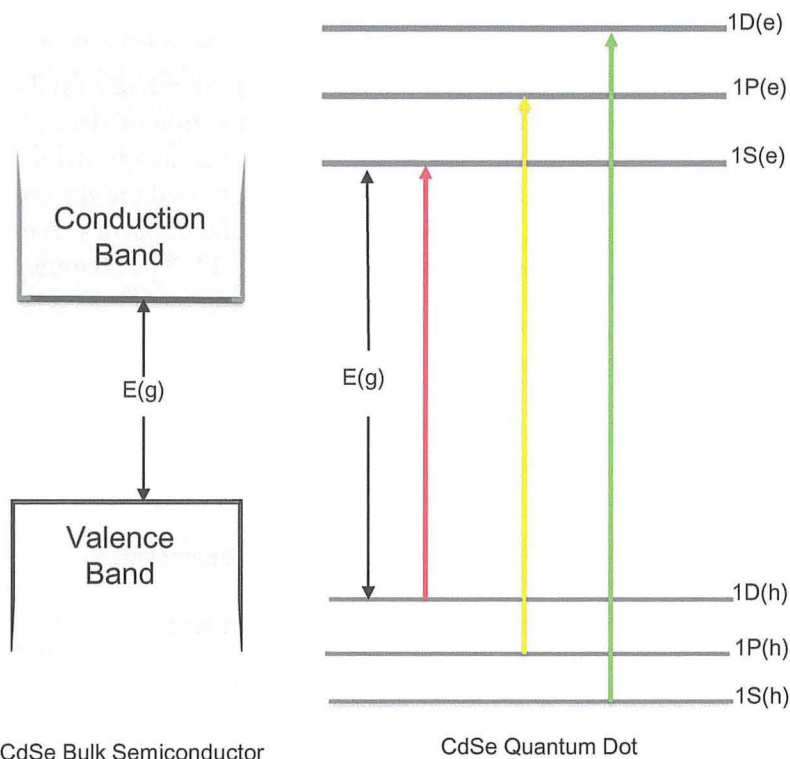
Fig. 13 Bulk semiconductors can absorb light at a spectrum of wavelengths, but as the size of the crystal reduces, discretization of energy levels takes place, and they absorb and emit light of only specific wavelengths. The wavelength of photons emitted by the quantum dot depends on its size. The smaller the size of the quantum dot, the larger the gap between the energy levels with confined excitons and the smaller the wavelength of photons emitted.

and/or material composition of the dots. The strength of the confinement can be divided into three categories:

- **Strong Confinement:** The Bohr radius for both the electron and hole is larger than the radius of the quantum dot, making the individual motions of the electron and the hole quantized. This confinement regime is defined for the smallest of the quantum dots.
- **Intermediate Confinement:** The Bohr radius of the electron is larger than the radius of the quantum dot, but the Bohr radius of the hole is smaller than the radius of the dot. With the effective mass of the holes being much bigger than the electrons, such confinement takes place.
- **Weak Confinement:** The Bohr radius of both the electron and hole is smaller than the radius of the quantum dot. This regime is appropriate for relatively large quantum dots.

4.2 Working principle

When an optical pulse illuminates the electrons in the valence band of the QD, they perform band jumps that lead to the formation of electron–hole pairs, which then transition back to the lowest-lying energy states of the respective bands (valence and conduction) rapidly. It results in the emission of photons corresponding to the transition energy and frequency. A general experimental setup for this process is shown in Fig. 14. The recombination
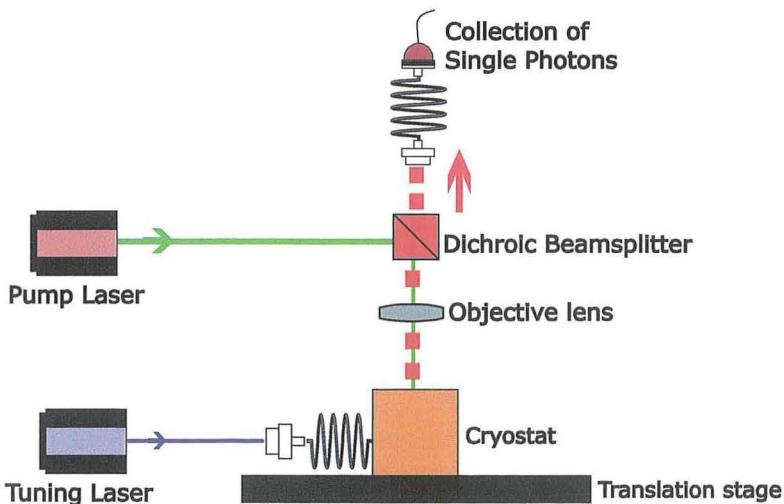

Fig. 14 Single-photon generation by focusing a laser beam onto the quantum dots and separating the photons and the pump beam using a dichroic beamsplitter. The cryostat provides a suitable temperature for quantum dots to emit. Quantum dots are classified on the basis of synthesis and operating temperature in the next section.

from the exciton (X), the biexciton (XX0 or XX), and the multiexciton (XXN) state where N refers to the number of electron–hole pairs left to recombine is observed depending on the population. All the transitions possess distinct energies and can be observed in the photoluminescence spectra of the Quantum Dot. Spectral filtering allows us to use emissions of a single wavelength (Sinha, 2023). The most commonly used transitions are the biexcitonic and the excitonic transitions, as shown in Fig. 15.

It can be seen using high-resolution spectroscopy that the XX and X transitions are doublets containing linearly polarized components. The asymmetry in the electron–hole exchange of the dot causes polarization splitting. If the pulse width of the exciting laser pulse is shorter than the lifetime of the exciton state ($\sim 1 ns$), then only one X photon is emitted per laser pulse. The state of the artquantum dots cannot inherently produce entangled photons, but if both the biexciton and exciton transition photons are collected, they can be used to generate entangled photon pairs. Hence, the output will be a statistical mixture of $|H_{XX}H_X\rangle$ and $|V_{XX}V_X\rangle$ photon states. Different methods have been employed to remove the spin splitting of the exciton state as it distinguishes the H- and V-polarized pairs (Tartakovskii, 2012).

4.3 Quantum dot preparation

Quantum dots can be classified into two broad classes based on synthesis: colloidal dots and epitaxial dots. Several methods have been adopted to synthesize QDs for various applications. Generally, the techniques used for QD synthesis are top–down and bottom–up approaches. The bottom–up approach includes the preparation of QDs by self-assembly in a solution following a chemical reduction (Yan et al., 2020). Colloidal quantum dots are produced via such wet chemical synthesis in which the solution is heated or precipitated to decompose the structures to monomer level and then to nanometer range crystals (Chen et al., 2019). The nucleation and growth of nanocrystals take place in a controlled manner. Wet-chemical synthesis generally includes electrochemistry, microemulsions, sol–gels, competitive reaction chemistry, hot-solution decomposition, sonic waves, and microwaves. Temperature and concentration of monomers are important factors in the optimal growth of these nanocrystals. They exhibit high quantum efficiency and photostability at room temperature and have a low fabrication cost. This method is useful for commercial applications as the colloidal dots can be prepared in large batches. The most common materials for this purpose are Indium arsenide, Lead sulfide, Lead selenide, and Cadmium sulfide (Hwa, Ganguly, Santhan, & Sharma, 2022). Recent advancements show
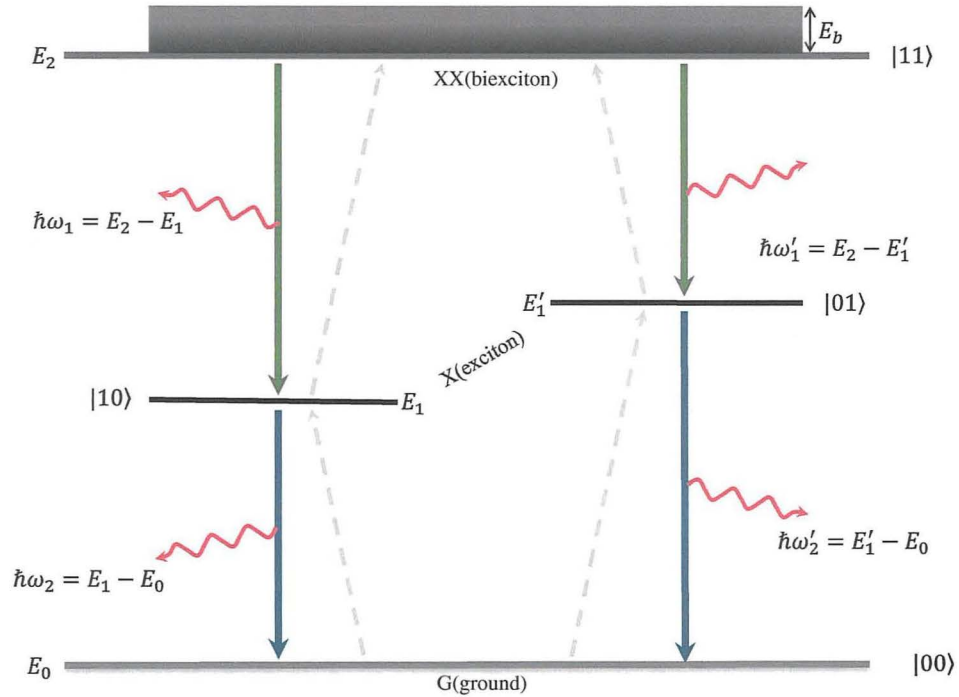
Fig. 15 The energy level diagram describes the formation of the exciton X and the biexciton XX states.

that it is possible to grow quantum dots from Calcium Titanium oxide minerals as well. Epitaxially grown quantum dots are produced spontaneously using top-down techniques such as laser ablation, liquid/vapor phase epitaxy (liquid and gaseous precursors are condensed on the surface of the substrate), molecular beam epitaxy (MBE, the beams of atoms/molecules are fired at a "base" or substrate such that a single crystal builds up slowly), ion implantation (ions are accelerated electrically and fired at a substrate), e-beam lithography (atomic-scale engraving using electron beams), and X-ray lithography (atomic-scale engraving using X-rays) (Borah, Mostako, Borgogoi, Saikia, & Malakar, 2020) via Stranski–Krastanov growth mode and emit single photons at cryogenic temperatures (Anderson et al., 2021). In top-down approaches, a bulk semiconductor is thinned to create QDs, while in bottom-down approaches, layers are grown in an atom-by-atom process (Sala, Godsland, Trapalis, & Heffernan, 2021). The self-assembly of QDs on a substrate occurs without any patterning. MBE is mainly used to self-assemble QDs from III–V semiconductors and II–VI semiconductors using the large lattice mismatch (Hodgson et al., 2018). MBE method also provides a unique possibility to produce quantum dot arrays with ultra-small dispersion of the size distribution function and to study the quantum size effect. Electron beam lithography, reactive-ion etching, and/or wet chemical etching are frequently employed to produce QDs with a diameter of about 30 nm. With the necessary packing geometries, QDs with controlled shapes and sizes can be prepared for systematic experiments on the quantum confinement effect (Liu et al., 2020). As an alternative to the above-mentioned processes, clusters of quantum dots can also be created using ion or laser beams. Plasma synthesis (Ma et al., 2019) is also a candidate for quantum dot production. Parameters like the shape, size, and surface of the quantum dot can be modulated better using this technique. It is advantageous over colloidal growth because of the challenges faced while doping. Silicon and germanium quantum dots can also be synthesized through nonthermal plasma.

Core–shell quantum dots and quantum dot films are two major categories of epitaxially grown quantum dots. Core–shell quantum dots have a thin shell (less than 10 nm) of a wide bandgap semiconductor material around the core semiconductor material (Shwetharani, Nayak, Jyothi, & Geetha Balakrishna, 2020) as shown in Fig. 16 (Clapp et al., 2004). The shell material stabilizes the growth of dots and passivates the nonradiative recombination processes in the core material, providing photostability. Organic ligand molecules cap the structure to prevent clumping and formation of larger particles.
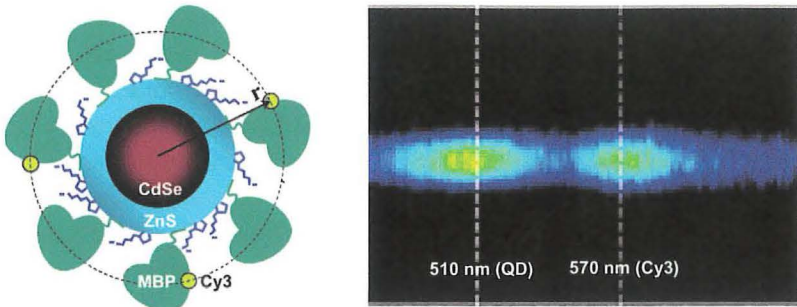
Fig. 16 (*Left*) Schematic representation of the bioconjugate QD-MBP-dye nano assembly and $\sim$ 15 proteins are immobilized on each QD surface (*Right*) Image showing the QDs with 3 MBP/7 MBP-Cy3 is emitting at 510 nm. *Adapted with permission from Clapp, A. R., Medintz, I. L., Mauro, J. M., Fisher, B. R., Bawendi, M. G., & Mattoussi, H. (2004). Fluorescence resonance energy transfer between quantum dot donors and dye-labeled protein acceptors. Journal of the American Chemical Society, 126(1), 301–310.*

Table 5 State of the art for QD-based photon sources concerning nature of the source, emission range, bandwidth, operating temperature, emission direction, and efficiency.

Probabilistic/ deterministic	Emission range	Bandwidth	Operating temperature	Emission direction	Efficiency
Deterministic	IR, telecom	nm	Room temp., cryogenic	Random, narrow	0.97 (Press et al., 2007)

Table 6 State of the art for QD-based photon sources with reference to brightness, $g^{(2)}$, entanglement fidelity, HOM visibility, and applications in quantum science and technologies.

Brightness	Best $g^{(2)}$	Entanglement fidelity	HOM visibility	Quantum applications
28.3 MHz (Chen, Zopf, Keil, Ding, & Schmidt, 2018)	0.000075 (Schweickert et al., 2018)	0.987(8) (Schimpf et al., 2021)	0.9956 (Somaschi et al., 2016)	Foundations and communications

QD films, also referred to as quantum dot arrays, are thin films containing localized clusters of atoms, each behaving like a quantum dot (Kim et al., 2020). Apart from semiconductor materials, graphene has also emerged as a potential candidate for quantum dot growth in recent years. It is possible to carve out nanoscale electronic devices from a single graphene crystal (Zhao et al., 2018) (i.e., graphene quantum dots) because it retains high photo–stability and conductivity even at that size scale. Synthesis of graphene quantum dots with controllable surface properties and tunable emission wavelength is an emerging field of research. State–of–the–art parameters for QD-based sources are mentioned in Tables 5 and 6.

- The operating temperature, as mentioned in Table 5, is cryogenic for epitaxial quantum dots and room temperature for colloidal quantum dots.
- 28.3 MHz (Chen et al., 2018) mentioned in Table 6 is the number of photon pairs collected from a single quantum dot.

5. Single-photon emitters in color centers

The quantum optics community has been interested in optically active defects for the past few decades. Point defects or point defect clusters in normally transparent materials are commonly referred to as color centers. Nitrogen- and silicon-vacancy centers in diamond (Riedrich-Moller et al., 2014), F-centers in NaCl (Wikipedia contributors, 2022), and defects in hexagonal boron nitride(h-BN) (Tran et al., 2016) and Silicon Carbide (Castelletto & Boretti, 2020) are examples of widely used color centers. The defects in the diamond crystal structure formed by a vacancy in the carbon lattice coupled with a substitutional noncarbon atom at an adjacent position are called vacancy centers in diamonds. Such changes in the crystal lattice lead to the emergence of localized energy states in the band structure of the material, which serve as isolated artificial atoms incorporated into a solid-state system. Vacancy centers in diamond have emerged as unique candidates for the implementation of solid-state single-photon emitters without the need for cryogenic operation as they show stable photon emission at room temperature, the lower probability for phonon–induced dephasing, and phonon-assisted emission due to extremely high Debye temperature of diamond (Davies, Hamer, & Price, 1976). In diamonds, more than 500 color centers have been found, and more than 10 of these have shown single-photon emission. We shall go into great detail on nitrogen–vacancy (NV) centers in diamonds in this section.

5.1 Nitrogen-vacancy centers

NV centers in diamonds are one of the important physical systems for emergent quantum technologies. The detection of single negatively charged nitrogen-vacancy (NV^-) centers in diamonds (Hanzawa, Nisida, & Kato, 1997) represents an important achievement in the development of diamond-based quantum technologies. The detection of NV centers soon enabled demonstrations involving photostable single-photon emission.

The NV center in diamond has C_{3v} symmetry and a pair of substitutional nitrogen-lattice vacancies oriented in the direction of the [111] crystalline
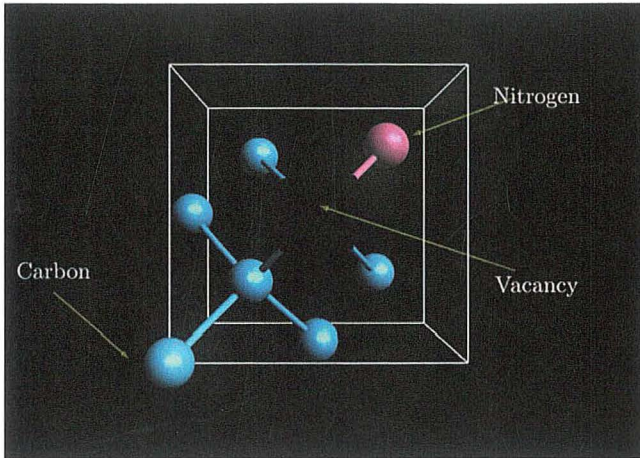
Fig. 17 Diagram of a nitrogen-vacancy center with a diamond lattice that shows the vacancy (in *black*), the carbon atoms that are closest to it (in *blue*), and the substitutional nitrogen atom (*purple*). *Adapted with permission from Sinha, U. (2023). Photon sources for quantum technologies, encyclopedia of materials: Electronics (1st ed.). Elsevier. https:// www.elsevier.com/books/encyclopedia-of-materials-electronics/abdul/978-0-12-819728-8. ISBN 9780128197288.*

structure (Fig. 17). Chemical vapor deposition (CVD), diamond synthesis, radiation damage, ion implantation, and annealing in bulk and nanocrystalline diamond may produce the center as an "in-grown" byproduct. In neutral charge states and negative charge states, the center is known to exist. The optical zero phonon lines (ZPLs) of NV^- and NV^0, which are at energies of 1.945 eV (637 nm) and 2.156 eV (575 nm), respectively, and associated vibronic bands that extend from their ZPLs to energies of higher/lower energy in absorption/emission (Kurtsiefer, Mayer, Zarda, & Weinfurter, 2000; Larsson & Delaney, 2008), serve as the distinguishing characteristics of these two charge states.

It has been determined that the $NV-$ center is responsible for another infrared ZPL at 1.190 eV (1042 nm) that can only be seen under optical illumination (with energy more than 1.945 eV). Sharp ZPLs with linewidths of a few THz at room temperature and clearly defined vibronic bands of NV^0 and NV^- show that the optical transitions take place between discrete defect levels that are far inside the diamond band gap, excluding the continuum of valence or conduction band levels from the process. Thus, the NV center is a deep-level defect in diamonds. The energy level diagram of the NV center is depicted in Fig. 18.
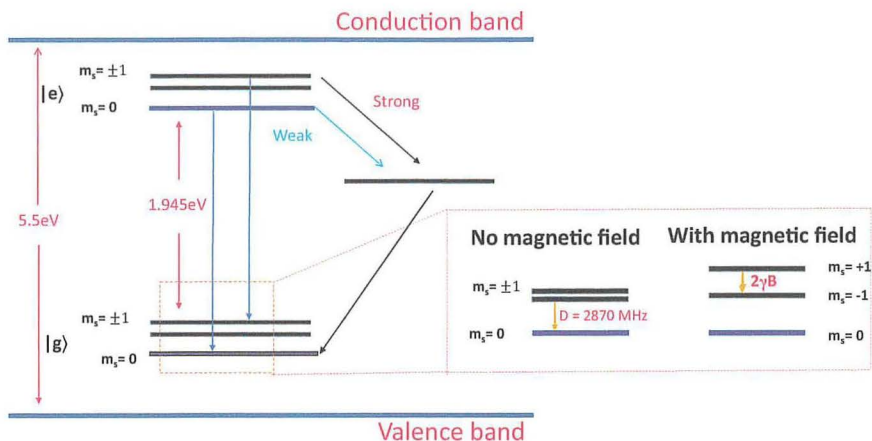
Fig. 18 Energy level diagram for NV^-. The *bold black line* shows the metastable singlet state, $|g\rangle$ the ground state, and $|e\rangle$ the excited state. The radiative transitions are indicated by the *blue arrows*, while strong and weak nonradiative decays via the singlet state are indicated by *black* and *sky blue arrows*, respectively. The three spin sublevels with $m_s = 0$ and $m_s = \pm 1$ at zero and nonzero magnetic field B are shown in the box in the right. D is the zero-field splitting, and $2\gamma B$ is the Zeeman splitting, where γ is the electron gyromagnetic ratio. Conventionally, $m_s = -1$ is linked to the lower energy transition (Figure courtesy: Ashlin Jacob, RRI Bangalore).

5.2 Physical and electronic structure

The tetrahedral structure of the diamond crystal lattice is made up of carbon atoms that are covalently bound to one another. In diamonds, nitrogen is the most common impurity to be found. Therefore, NV centers can be produced either naturally or artificially. The NV axis and the nearby carbon atoms have a 109.5 degrees bond angle which is same as the pure diamond. The structure of the NV center is rotationally symmetric about the NV axis by an angle of 120 degrees.

Six electrons make up the NV center's electronic structure. Two of these come from the nitrogen atom, and three come from the dangling bonds formed by the carbon atoms surrounding the vacancy. The lattice's sixth electron is snatched (usually by nitrogen donors), changing the overall charge state to NV^-. The three carbon atoms and the empty site have the maximum electron densities, which are generally positioned in a plane vertical to the major NV axis. Despite the existence of the neutral NV^0 and positively charged NV^+ charge states, neither is magneto–optically active. The negative NV^- charge state is used in every experiment on NV centers.

5.3 Optical properties

The NV center absorption spectrum ranges from 450 to 650 nm, peaking at 555 nm. As a result, 532 nm visible laser pulses can be employed for excitation. The emission band has a stable photoluminescence (Manson, Harrison, & Sellars, 2006) and lies within 600 to 850 nm. A natural type Ib diamond crystal with a size of the order of millimeters has been reported to have an excited state lifetime of 13 ns. NV centers' fluorescence in diamonds can be imaged using a confocal microscope. Three electronic levels can be used to describe the photophysics of NV centers, including a ground state $|g\rangle$ with the symmetry $^3A_2$, an excited state $|e\rangle$ with the symmetry ^3E, and a metastable singlet state $|s\rangle$ that involves two levels with the symmetries $^1A_1$ and ^1E (Fig. 18).

The ground and excited states are divided into three spin sublevels and are spin triplets ($S = 1$). The primary $|g\rangle\rightarrow|e\rangle$ transition can be efficiently excited at most wavelengths below 640 nm (Gali, 2019; Weerdt, Collins, Zugik, & Connor, 2005). Its resonant wavelength is 638 nm (ZPL). The majority of luminescence occurs in vibrational sidebands between 630 and 800 nm (Fig. 19), with just a small number of photons being emitted into the zero phonon line. Due to their varying refractive indices, the radiative lifetime is different for NV centers in different sizes of diamond crystals. The
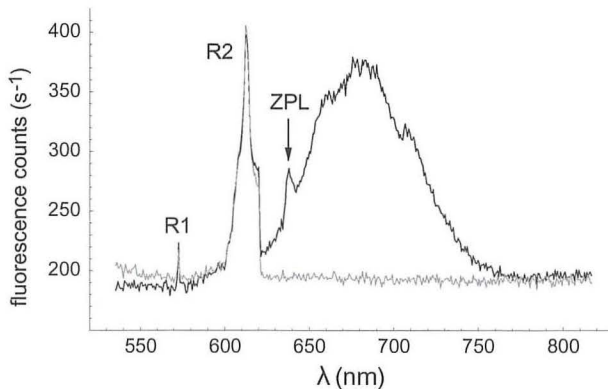
Fig. 19 Single NV center's fluorescence spectrum (in *black*) and a reference spectrum from an empty region in a type 1b diamond (*gray*). At 637 nm, between the NV center's vibrationally broadened spectrum, the ZPL line is clearly visible. The vibrational spectrum also exhibits a kink that can be seen in the (R1) and (R2) spectra from two-phonon Raman scattering. *Adapted with permission from Kurtsiefer, C., Mayer, S., Zarda, P., & Weinfurter, H. (2000). Stable solid-state source of single photons. Physical Review Letters, 85(2), 290–293. https://doi.org/10.1103/PhysRevLett.85.290.*

radiative lifetime of the excited state for NV centers in bulk diamonds is around 13 ns, and for NV centers in nanodiamonds is roughly 25 ns. The metastable singlet state has a lifetime of about 250 ns. The quantum yield, which ranges from 70% to 80% depending on the spin state, is the proportion of excited electrons that decay by the radiative triplet–triplet transition.

Many quantum optics investigations involve the fluorescence of two-level quantum systems. They are suitable for single-photon generation due to their high quantum efficiency, which is nearly close to one even at room temperature, and the very short decay time of the excited state. The fluorescence of NV centers in synthetic Ib diamond indicates clear signs of nonclassical light. Strong photon antibunching can be seen for very small differences in detection periods, which makes this system an excellent choice for single-photon creation by pulsed excitation. The main characteristics that set NV centers apart from other fluorescing quantum systems are their resistance to photobleaching and the all-solid-state configuration. The implementation of optical quantum information processing methods and quantum cryptography protocols depends on photon sources that can create single-photon pulses on demand (Gisin, Ribordy, Tittel, & Zbinden, 2002). Tables 7 and 8 list many state-of-the-art parameters of NV centers-based sources.

- Count rate 4.56 MHz reported in Table 8 is for a source with $g^2(0) = 0.1$ at low excitation power (Andersen et al., 2017 a), while 850 kHz brightness is reported for a source with $g^2(0) = 0.08$ (Andersen et al., 2017 b).
- Recently, a very low $g^2(0)$ value of 0.0168 was reported for silicon vacancy (SiV), based source in diamonds (Knall et al., 2022).
- A very high count rate of 0.1 GHz was reported for a source based on $Si_C - SF$ defects in silicon carbide and inferred count rate of 5GHz (Khramtsov, Vyshnevyy, & Fedyanin, 2018). The $g^2(0)$ value for the said

Table 7 State of the art in terms of source type, emission range, bandwidth, operating temperature, emission direction, and efficiency for NV center-based photon sources.

Probabilistic/ deterministic	Emission range	Bandwidth	Operating temperature	Emission direction	Efficiency
Deterministic	600–800 nm (Leifgen et al., 2014)	1–100 nm	300–500 K	Random, narrow (wu, Liu, Chen, & Li, 2010)	0.90 (Schrinner, Olthaus, Reiter, & Schuck, 2020)

Table 8 State of the art in terms of brightness, $g^{(2)}$, entanglement fidelity, HOM visibility, and applications in quantum research and technology for NV-based photon sources.

Brightness	Best $g^{(2)}$	Entanglement fidelity	HOM visibility	Quantum applications
4.56 MHz (Andersen, Kumar, & Bozhevolnyi 2017 a), 850 kHz (Andersen, Kumar, & Bozhevolnyi, 2017 b)	0.07 (Beveratos et al., 2002)	0.70±0.070 (Humphreys et al., 2018)	0.66 (Bernien et al., 2012)	Foundations and communications

source was <0.1 with background corrections and ~0.2 without background corrections (Lohrmann et al., 2015). The lifetime of the excited state, shelving state, and quantum efficiency was quoted to be the reasons for limiting the emission rate.

6. Applications

The sources discussed in this chapter find applications in a spectrum of fields starting from proof of fundamental laws in quantum mechanics (Sinha et al., 2009) to quantum communications, computing, metrology (Polino, Valeri, Spagnolo, & Sciarrino, 2020), imaging (Berchera & Degiovanni, 2019), sensing (Pirandola, Bardhan, Gehring, Weedbrook, & Lloyd, 2018), and diagnostics applications (Díaz-González, de la Escosura-Muñiz, Fernandez-Argüelles, Alonso, & Costa-Fernandez, 2020). In this section, we will discuss the applications of these photon sources in detail in the field of quantum communications and quantum computing. Quantum communication-based applications can be further categorized into quantum key distribution (QKD) and nonkey distribution applications, i.e., quantum teleportation (QT) and remote state preparation (RSP).

6.1 Quantum key distribution

Currently, the security in classical communication is provided by the hardness of mathematical computation. With the evolution of quantum technologies and algorithms using fundamental laws of quantum mechanics, classical cryptography is no longer secure and can be broken with ease. Using these laws of quantum mechanics itself, it is possible to develop an architecture for secure quantum communications. Various techniques of cryptography to achieve secure communications have been tested. The "one-time pad" method of encryption and decryption works very well, given a secure

key has already been distributed among the sender and the receiver. The area of research focusing on the distribution of the key, in other words, a string of bits for encryption and decryption, is known as quantum key distribution. QKD schemes using photons are mainly classified into two categories, i.e., prepare and measure-based and Quantum Entanglement-based protocols. Experimental implementation of such protocols requires either a single-photon source or sources producing entangled photon pairs. Now, we will discuss the developments in QKD architecture over the years in light of the photon source used in the experiment.

Spontaneous parametric downconversion (SPDC)-based single-photon sources are well established and explored in terms of brightness, very low $g^{(2)}$ value, high entanglement fidelity, and several other parameters as discussed before. Therefore, SPDC-based photon sources are a common choice for quantum key distribution experiments using photons. The first ever QKD protocol proposed was the BB84 protocol. The proof-of-principle experiment for BB84 was performed in 1989 by Bennett and Brassard (1989), the same computer scientists who proposed the BB84 protocol in 1984. They could share 403 quantum bits perfectly with an estimation of about 5% of error in the protocol. In 1998, Buttler et al. developed a working QKD setup over a free space link of 205 m in-lab optical path under fluorescent lighting conditions, which laid the foundation of the vast field of free space secure communications. This was followed by an outdoor demonstration of QKD using B92 protocol over a quantum channel 1 km long by the same research group toward the latter part of 1998. In 2006, Marcikic, Lamas-Linares, and Kurtsiefer (2006) demonstrated BB84 QKD protocol experimentally over a 1.5 km distance using polarization-entangled photon pairs generated using an SPDC-based source. An average key rate of 630 bits/s with a QBER of 5.75% after error correction and privacy amplification was reported. Development and demonstration of entanglement-based protocols promised enhanced security for communications over longer distances by exploiting the quantum correlations of the particles.

BBM92 is a quantum key distribution protocol where the security is largely based on the entanglement present in the shared photon pair between Alice and Bob (sender and receiver). The first experimental implementation of BBM92 was reported in the year 2000 (Jennewein, Simon, Weihs, Weinfurter, & Zeilinger, 2000), generating a key rate of 400–800 bits/s with a quantum bit error rate (QBER) of 3% with 360 m of separation between the two parties. In 2008, Erven, Couteau, Laflamme, and Weihs (2008) used the BBM92 protocol to share the key over two free-space optical telescope

links with a combined distance of 1.575 km. A type II SPDC source was used, and a 565 bits/s key rate was reported with a QBER of 4.92%. In such long-distance communication, timing synchronization is crucial. The protocol was time synchronized at different locations by using GPS timing receivers and time taggers. A. K. Ekert, in 1991, proposed a QKD protocol named Ekert91 or E91 using nonlocal correlations between maximally entangled photon pairs. The first experimental demonstration of the E91 protocol was reported in 1998 (Ling, Peloso, Marcikic, Lamas-Linares, & Kurtsiefer, 2008). Violation of a Bell inequality was used to derive a secure key with a key rate of 200 bits/s and QBER of 4%. In 2009, Zeilinger's group (Scheidl et al., 2009) communicated securely over 144 km and theoretically verified the possibility of repeating the same protocol using similar methods for over a 300 km link. Long-distance quantum communications have been explored and protocols have been implemented over 1200 km now. Satellite-ground quantum key distribution via BB84 protocol (Liao et al., 2017), as well as entanglement-based protocols (Yin et al., 2017), has been demonstrated for a distance range of 500–1000 km using an SPDC-based source. Realizing an experimental photonic QKD protocol requires complex optical alignment and a large amount of resources. Thus, it is advantageous to simulate any protocol before its experimental implementation. In 2020, the Sinha group at Raman Research Institute Bangalore came up with qkdSim (Chatterjee, Joarder, Chatterjee, Sanders, & Sinha, 2020), a toolkit enabling QKD experimentalists to pre-analyze the performance of an experimental setup for a QKD protocol by estimating the key rate, QBER, and key symmetry while considering the realistic imperfections in the experimental setup. In the same work, they reported the experimental implementation of B92 QKD protocol using a type-II SPDC source and obtained a key rate of 51.0 ± 0.5 and QBER of $4.79 \pm 0.01\%$ which is lower than the theoretical QBER threshold for the B92 protocol (i.e., 4.8%). Above mentioned experiments used particle properties corresponding to a two-dimensional Hilbert space. Recently successful demonstrations were reported for QKD experiments in higher dimensions as well. One such demonstration is a fiber-based BB84 experiment by Vagniluca et al. over 145 km in a four-dimensional Hilbert space in 2020 (Vagniluca et al., 2020).

Entangled photons built using four-wave mixing inside photonic crystal optical fibers (McMillan et al., 2009) can be propagated easily to establish optical networks at telecommunication wavelength as the otherwise significant coupling losses are nonexistent in this case. Multiphoton emission can

also be controlled depending upon the fiber source parameters such as pump power, fiber length, fiber nonlinearity coefficient, phase mismatch, and the efficiency of the photon number measures used. The photon number distribution of the emission can be determined using the quantum theory of FWM and Wigner functions of the resultant photons. It gives a way to analyze the efficiencies of the quantum key distribution with the above-mentioned photon sources (de Brito & Ramos, 2010). Although there are proposals that suggest the possibility of quantum cryptography in optical fibers and free space using degenerate FWM-based sources (de Brito & Ramos, 2010; Liñares, Prieto-Blanco, Balado, & Carral, 2021), there is not enough experimental evidence of the same. Higher background counts brought on by spontaneous Raman scattering (SRS), which results in reduced heralding efficiency, is one of the main reasons for this. Cooling the fibers is one method of lowering SRS. Although cooling the fiber is physically challenging, the population in vibrational modes is reduced at lower temperatures, resulting in lower dispersion. Moving the signal/idler frequency far away from the Raman peak is another option. Moreover, fiber FWM turned out to be a dominant source of background noise in a reconfigurable optical add/drop multiplexer network-based QKD where the 1550 nm QKD signal was multiplexed with neighboring degenerate wavelength division multiplexing (DWDM) channels. In an experimental implementation of BB84 protocol using the above-mentioned multiplexing network, QBER was found to be 9.8% at a secure key rate of 107 b/s (Toliver et al., 2007). The higher-than-expected QBER was due to cross talks between the different frequency components of the network resulting from four-wave mixing inside the fiber.

In 2013, Liu et al. (2013) demonstrated the first proof-of-principle differential-phase-shift QKD experiment (Inoue, Waks, & Yamamoto, 2002) using narrow-band photon pairs generated by FWM in a magneto-optical trap. The QBER reported was 3.06% which satisfied the unconditional security requirement of the said protocol (Wen, Tamaki, & Yamamoto, 2009).

Although deterministic single-photon sources came into existence quite recently in comparison to the probabilistic sources, their integration into already existing quantum protocols has been quite appreciable. Quantum dots made their way into the regime of quantum communications, previously dominated by SPDC sources, in the early 2000s. Intallura et al. (2007) performed the first quantum key distribution experiment (an implementation of BB84 protocol) that used a Quantum dot as a source of single photons in 2007. This implementation distributed a 7 kbit sifted key over a

distance of 35 km with a QBER of 5.9% using an Indium Arsenide (*InAs*) Quantum dot (emitting at 1300 nm) in a pillar microcavity as a source. Over time as high purity sources and detectors with more efficiency and fewer jitters like superconducting nanowire single-photon detectors (SNSPD) came into play, the distance for implementation, the raw key rate, and QBER improved from 50 km, 14.5 to 101.8 bps, and 4.8–6.2%, respectively in 2010 (Takemoto et al., 2010) to 120 km, 34.3 bps, and 2.3% in 2015 (Takemoto et al., 2015) over a telecommunication optical fiber for quantum dots with optical horn structure. In 2012, Heindel et al. (2012) extended the quantum dot source-based QKD implementations to the free space regime. The sifted key rates of 27.2 kbit/s at a QBER of 3.9% were reported for a source of $g^{(2)}(0)$ value of 0.35 emitting in the near-infrared region over a distance of 40 cm. They also reported the sifted key rates of 95.0 kbit/s at a quantum bit error rate QBER of 4.1% for a source of $g^{(2)}(0)$ value of 0.49 emitting at red wavelength in the same demonstration. Due to the ability of quantum dots to produce on-demand single photons and emit polarization-entangled photons with very low multiphoton emissions even at high brightness, they are a suitable choice for entanglement-based key distribution protocols. In 2015, Dzurnak et al. (2015) performed a BBM92 protocol using *InAs* quantum dots and obtained a sifted key rate of 0.17 bits/s and QBER of 9.8% which is lesser than the 11% threshold of error correction algorithms but has a lot more room for improvement. The lowest QBER reported so far for QKD demonstrations using QD-based photon sources is 1.9% with a raw and secure key rate of 135 and 86 bits/s, respectively, over a span of 13 h for a key generated using BBM92 protocol and distributed over 350 m using an optical fiber in 2021 (Schimpf et al., 2021). Recently, quantum key distribution has been successfully demonstrated in broad daylight, cloudy, and rainy weather conditions. One such experiment was performed by Basset et al. (2022), over a span of three and a half days across a 270 m free space optical link. They reported a sifted key rate of 106 bits/s and a QBER of 7.16(2)%.

Apart from quantum dots, various color centers are employed as deterministic single-photon emitters in quantum communication-based applications. In 2002, Basset et al. (2022) demonstrated the first QKD protocol using nitrogen-vacancy centers in diamond nanocrystals as a single-photon source (Beveratos et al., 2002). An implementation of BB84 protocol was reported with a QBER of 4.6% and a secure key rate of 7700 bits/s over a free space link of 50 m. In 2004, the same group tested the performance of the above-discussed system as a function of added attenuation to the quantum channel (Alléaume et al., 2004). It was shown that the QBER gradually

increases, starting from 1.65% to 9.4%, as the attenuation in the quantum channel increases. The added attenuation mimicked the losses that will come into play on increasing the distance between the sender and the receiver. The single-photon sources based on NV centers suffer drawbacks because of the emission of partially polarized light at room temperature, broad emission spectrum, and long lifetime of the excited state (Neu & Becher, 2014). Due to these shortcomings, the research community started exploring other color centers for quantum communication applications. Silicon–vacancy centers in diamonds emit photons of a high degree of polarization and have a short lifetime. In 2014, Leifgen et al. (2014) demonstrated BB84 protocol using photons generated from NV and SiV centers in diamond in a QKD testbed and presented a comparison study. A QBER of 3.0 ± 0.2 % and secure key rate of 2.6 kbits/s was reported for the QKD demonstration with NV center-based source and QBER of 3.2 ± 0.2 % and a secure key rate of 1 kbit/s was reported for the QKD demonstration with SiV center-based sources where both the sources had a repetition rate of 1 MHz. Although the QBER in both cases is similar, the secure key rates in the case of SiV center-based sources are lesser than NV center-based sources. The study concludes that it is easier to suppress multiphoton effects in the case of SiV center-based sources, and the key rates can be increased by increasing the brightness of the source. Similarly, many single-photon sources based on various color centers are being exploited to make them compatible with quantum communication applications. In 2022, Samaner, Paçal, Mutlu, Uyanık, and Ateş (2022) demonstrated a B92 QKD protocol using single photons generated from an isolated defect in hexagonal-boron nitride (Samaner et al., 2022). They reported a QBER of 8.95% and a sifted key rate of 238 bits/s. NV centers in diamonds can be used as quantum memories in memory-assisted schemes for long-distance QKD as it helps to beat the existing no-memory schemes in terms of key rate versus distance (Lo Piparo, Razavi, & Munro, 2017). NV center-based quantum memories are quite reliable because the electronic spins of NV centers have a higher coherence time of the order of milliseconds which can also be extended up to seconds if nuclear spins are used. Their low interaction time with photons also provides an advantage over other systems. NV-centers in diamonds are also one of the most suitable candidates for quantum sensing (Radu et al., 2019).

6.2 Quantum teleportation

Quantum teleportation is an information transfer protocol proposed by Charles Bennett in 1993 (Bennett et al., 1993). A quantum teleportation

protocol sends the quantum information encoded in the state of the particle onto another particle separated by a distance. Let's say a physical distance separates Alice and Bob, and Alice needs to send an unknown quantum state to Bob. This unknown state can be a spin state of an electron or a polarization state or the orbital angular momentum degree of freedom of photons. Alice (sender) and Bob (receiver) are connected by a quantum channel as well as a classical channel. A quantum channel comprises a pair of photons entangled in polarization degree of freedom generated using either of the techniques described in this chapter. One of the entangles photons is with Alice, and the second is given to Bob. In an all-photonic system, the unknown polarization state of an input photon can be written as

$$|\phi_1\rangle = \alpha|0_1\rangle + \beta|1_1\rangle, |\alpha|^2 + |\beta|^2 = 1 \qquad (41)$$

The bipartite state in which the other two entangled photons can be prepared is one of the Bell states

$$|\psi_{23}^-\rangle = \frac{1}{\sqrt{2}}[|0_2 1_3\rangle - |1_2 0_3\rangle] \qquad (42)$$

where $|0\rangle$ and $|1\rangle$ are the eigenstates of the chosen polarization basis. The quantum state of the three-photonic system can be written as

$$|\psi_{123}\rangle = |\phi_1\rangle \otimes |\psi_{23}^-\rangle = \alpha|0_1\rangle + \beta|1_1\rangle \otimes \frac{1}{\sqrt{2}}[|0_2 1_3\rangle - |1_2 0_3\rangle] \qquad (43)$$

$$|\psi_{123}\rangle = \frac{\alpha}{\sqrt{2}}(|0_1\rangle|0_2 1_3\rangle - |0_1\rangle|1_2 0_3\rangle) + \frac{\beta}{\sqrt{2}}(|1_1\rangle|0_2 1_3\rangle - |1_1\rangle|1_2 0_3\rangle) \qquad (44)$$

where $|\psi_{23}^-\rangle$ is a nonseparable state. To send $|\phi_1\rangle$ to Bob, Alice needs to make a measurement. But a projective measurement will collapse the input state, and Bob trying to recreate the input state from the measurement outcomes might not lead to the same superposition coefficients. So Alice takes advantage of her part of the entangled pair and performs a joint Bell state measurement on photons 1 and 2 together, which projects the joint state of 1 and 2 into a maximally entangled state on a Bell basis. Bell basis consists of four orthonormal nonseparable bipartite states, and each of them has an equal probability of occurring in an ideal scenario.

$$|\psi_{12}^\pm\rangle = \frac{1}{\sqrt{2}}(|0_1\rangle|1_2\rangle \pm |1_1\rangle|0_2\rangle)$$

$$|\phi_{12}^\pm\rangle = \frac{1}{\sqrt{2}}(|0_1\rangle|0_2\rangle \pm |1_1\rangle|1_2\rangle)$$

One of the first used linear Bell state analyses in an optics lab was two–photon interference on a beamsplitter. Since photons 1 and 2 have been entangled due to joint projection into a nonseparable state, the entanglement between 2 and 3 vanishes.

$$|\psi_{123}\rangle = \frac{\alpha}{\sqrt{2}}(|0_1\rangle|0_2\rangle|1_3\rangle - |0_1\rangle|1_2\rangle|0_3\rangle)$$
$$+ \frac{\beta}{\sqrt{2}}(|1_1\rangle|0_2\rangle|1_3\rangle - |1_1\rangle|1_2\rangle|0_3\rangle) \tag{45}$$

$$|\psi_{123}\rangle = \frac{1}{2}[\left(\frac{1}{\sqrt{2}}|0_1\rangle|0_2\rangle\right)(\alpha|1_3\rangle) - \left(\frac{1}{\sqrt{2}}|1_1\rangle|1_2\rangle\right)(\beta|0_3\rangle)$$
$$+ \left(\frac{1}{\sqrt{2}}|0_1\rangle|0_2\rangle\right)(\alpha|1_3\rangle) + \left(\frac{1}{\sqrt{2}}|1_1\rangle|1_2\rangle\right)(-\beta|0_3\rangle)$$
$$+ \left(\frac{1}{\sqrt{2}}|0_1\rangle|1_2\rangle\right)(-\alpha|0_3\rangle) + \left(\frac{1}{\sqrt{2}}|1_1\rangle|0_2\rangle\right)(\beta|1_3\rangle)$$
$$+ \left(\frac{1}{\sqrt{2}}|0_1\rangle|1_2\rangle\right)(-\alpha|0_3\rangle) - \left(\frac{1}{\sqrt{2}}|1_1\rangle|0_2\rangle\right)(-\beta|0_3\rangle)] \tag{46}$$

$$|\psi_{123}\rangle = \frac{1}{2}[|\phi_{12}^-\rangle(\alpha|1_3\rangle + \beta|0_3\rangle) + |\phi_{12}^+\rangle(\alpha|1_3\rangle + \beta|0_3\rangle)$$
$$+ |\psi_{12}^+\rangle(-\alpha|0_3\rangle + \beta|1_3\rangle) + |\psi_{12}^-\rangle(-\alpha|0_3\rangle - \beta|1_3\rangle)] \tag{47}$$

Regrouping the photonic states as a superposition state of Bell basis for 1 and 2 shows that as soon as a measurement is made onto 2, photon three gets projected into the same basis as 1. After making this measurement, Alice communicates to Bob the result of her measurement through the classical channel and depending on which state 1 and 2 have been projected to. Bob performs a unitary transformation to get the input state back. These unitary transformations are 180 degrees rotations about the x, y, and z axis represented by σ_x, σ_y, and σ_z in quantum mechanics (Bennett et al., 1993). These operators can be created using a half-wave plate, a quarter-wave plate, and polarizing beamsplitter combinations in an optical setup. No cloning theorem (Wootters & Zurek, 1982) prevents making copies of a quantum state, the state gets destroyed from the sender's end as soon as it reaches the receiver. Hence, the name teleportation comes into play. In an ideal scenario, for every run of a teleportation experiment, the input state will be successfully transferred with unit probability. Thus, the fidelity of the protocol, which is a closeness of two quantum states, will always be one. If the protocol is implemented only using a quantum channel, then Bob will guess Alice's measurement result, and the output will not be the same as the input

state but a random mixture of four states in case of a 2×2 Hilbert space. This completely mixed state should contain no information about $|\phi_1\rangle$ as Bob creating the input state back before receiving the result of Alice's measurement classically would lead to faster-than-light communication which is prohibited by no-communication theorem.

The 2022 Nobel Prize in Physics has been awarded to Quantum information, and Anton Zeilinger's work on experimental quantum teleportation is very relevant to the scope of this chapter. His group performed the first proof-of-principle experimental implementation of quantum teleportation in 1997 (Bouwmeester et al., 1997). A BBO crystal was pumped with an Ultraviolet pulsed laser (394 nm) of duration 200 fs and repetition rate of 76 MHz, and pairs of downconverted entangled photons were generated at 788 nm with a bandwidth of 4 nm. The photons were entangled in the polarization degree of freedom and were represented by the antisymmetric Bell state. A photon of known polarization was used at the input, and a dip in threefold coincidence probability measurement between the two Bell state detectors and the detector at the receiver end confirmed the working of the protocol in this all-photonic setup. Later on, the same group performed this experiment over a distance of 600 m with a successful teleportation event rate of 0.04 per second (Ursin et al., 2004) at 788 nm across the river Danube in Vienna using an optical fiber. All the teleportation experiments were performed via an optical fiber link till 2010 when Jin et al. (2010) performed the first free space teleportation over a distance of 16 km and an averaged fidelity of 0.89. A free space link is crucial for the global quantum network and due to low atmospheric absorption, various near-infrared wavelengths are suitable for establishing these links. After 2 years, Zeilinger's group increased the distance of the free space link-based demonstration to 143 km between two islands with the fidelity of 0.863(38) (Ma et al., 2012). Both the above-mentioned free space experiments used a Type II BBO downconversion crystal to generate the pair of entangled photons. The longest distance over which SPDC-based teleportation has been demonstrated to date is 1400 km in a ground-to-satellite free space link by Pan's group at the University of Science and Technology of China in 2017 using Micius satellite (Ren et al., 2017), and the fidelity obtained was 0.80 ± 0.01. To build a global network, we need to develop techniques like quantum relays (Kaiser et al., 2014; Martin, Alibart, De Micheli, Ostrowsky, & Tanzilli, 2012) and quantum repeaters (Briegel, Dür, Cirac, & Zoller, 1998; Sangouard et al., 2008) to elongate the distance of these links without considerable absorption losses and maintain high fidelity.

Entanglement swapping is one such technique that forms the building block of quantum repeaters along with quantum memories. A long-distance link can be divided into smaller links, each containing a pair of entangled photons. Say A and B, and C and D are two pairs of entangled photons. If we perform a Bell state measurement over B and C, A and D will get entangled, and this can be used to elongate the distance between the sender and the receiver. Jin, Takeoka, Takagi, Shimizu, and Sasaki (2015) performed swapping at a high rate (fourfold coincidence count) of 108 counts per second using entangled photons generated by a type II group velocity-matched PPKTP crystal via SPDC at telecom wavelength and demonstrated teleportation through a fiber link with 0.763 fidelity.

Spontaneous parametric four-wave mixing (Horowicz, Pinard, & Reynaud, 1987), the nonlinear $\chi^{(3)}$ process in optical materials is widely used for the production of entangled photons. As discussed above, the quantum channel for quantum teleportation protocol is an EPR pair, and entangled photons generated by FWM are good candidates for the same. FWM can generate entangled photons inside optical fibers at telecommunication wavelength, which makes it inexpensive and readily compatible with communication technologies (Wang, Hong, & Friberg, 2001). Here, optical fibers act like waveguides and entangled photons are emitted in a single mode. The pair generation rate for FWM is higher than SPDC but also shows high SRS background counts, as discussed in the previous section. The average teleportation fidelity higher than 0.9 is attainable for hybrid entangled resources of purity lower than 0.8 with a wide spectrum in the telecommunications band (Domínguez-Serna, Rojas, & Garay-Palmett, 2020). Although these proposals seem reliable, there is no experimental evidence for the realization of QT using FWM-based sources so far.

As discussed earlier, QD-based sources have an advantage over SPDC and FWM-based sources because of the on–demand availability of emitted single photons, which makes it advantageous in implementing communication protocols. One of the first successful proof-of-principle experiments for Quantum teleportation using quantum dot sources was performed in 2004 with an average postselected fidelity of 0.80 using ancillary photons during Bell state measurement. The state-of-the-art values for average postselected fidelity are 0.883 ± 0.04 for quantum dots emitting at 1310 nm (telecommunication region, 2020; Anderson et al., 2020) and 0.842(14) for quantum dots emitting at 785 nm (near-infrared region, 2021; Basso Basset et al., 2021). Fig. 20 shows the experimental setup and fidelity curves for the highest recorded fidelity of QT using a QD-based source in the telecommunication region.
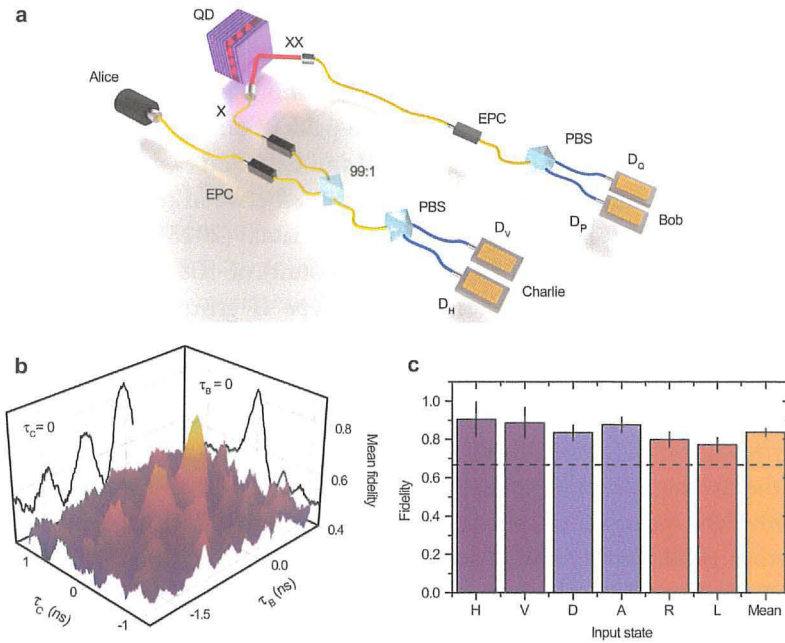
Fig. 20 Experimental schematic for teleporting a laser qubit is shown in (A). (B) The postselection window size's 203 ps average fidelity coincidence map. For the six input polarization states, the average fidelity (C) corresponds to the individual fidelities. The *dotted line* for each basis in the six-state teleportation protocol indicates that the fidelity surpasses the classical limit of 2/3. *Adapted with permission from Anderson, M., Müller, T., Huwer, J., Skiba-Szymanska, J., Krysa, A. B., Stevenson, R. M., …Shields, A. J. (2020). Quantum teleportation using highly coherent emission from telecom C-band quantum dots. npj Quantum Information, 6(1), 14. https://doi.org/10.1038/s41534-020-0249-5.*

Above mentioned experiments involved sending polarization state information from one photon to another. However, experiments have been conducted to extend this principle to teleport the photon state onto a spin state of an electron, as the underlying Hilbert space for both polarization and spin follow the same algebra (Gao et al., 2013; Qiao et al., 2020). This will help create quantum memories in the future as quantum dots are good candidates for computing and storing information in the naturally trapped electron spin states.

Given their capacity to produce remote entanglement, control many qubits per node, and read out multiple qubits simultaneously, NV centers are one of the most promising possibilities for creating a quantum network via teleportation. In the NV center teleportation scheme, Alice and Bob

each control a single NV center, and the photons produced eventually become entangled. NV centers are one of the most promising candidates for realizing a quantum network through teleportation because of their ability to generate remote entanglement and to control and read out multiple qubits per node. In the teleportation scheme using NV centers, Alice and Bob each control a single NV center, the photons generated by which are entangled with each other later. In 2014, quantum teleportation was demonstrated using electronic spins of NV centers in a diamond over a distance of 3 m obtaining a fidelity of 0.50 ± 0.03 without feedforward and 0.77 ± 0.03 with feedforward (Pfaff et al., 2014), but no photonic teleportation experiment using NV center has been reported so far.

6.3 Remote state preparation

In the remote state preparation (RSP) (Bennett et al., 2001) quantum communication protocol, Alice helps Bob to create a quantum state that she already knows due to shared entanglement and earlier classical communication. The asymptotic classical communication cost of RSP for general states at the high entanglement limit is one bit per qubit. However, there is no reliable RSP technique for a finite N number of states that consistently uses less classical communication than teleportation.

Here, it is feasible to make trade-offs between the amount of required entanglement and the expense of using classical communication (Bennett et al., 1993), in contrast to quantum teleportation, where the resources are fixed for the task. The measuring strategy Alice must use to carry out the protocol is a significant component that separates RSP from QT. Alice must perform a full Bell-state measurement (BSM) in QT. The measurement technique in RSP, however, is more flexible. Projective measurements may be sufficient in the simplest scenario, or Alice may need to implement a generalized measurement on her qubit.

Pati (2000) has put out the precise remote state preparation (RSP) protocol for a specific class of qubits. It was shown that one could remotely prepare a qubit selected from the equatorial or polar great circles of a Bloch sphere utilizing one classical bit of communication by using a pair of Einstein–Podolsky–Rosen (EPR) entangled states. Let's have a pure input state called $|\Psi\rangle$.

$$|\Psi\rangle = \alpha|0\rangle + \beta|1\rangle \tag{48}$$

where $\alpha = \cos\frac{\theta}{2}$ and $\beta = \sin\frac{\theta}{2}e^{(i\Phi)}$. They individually share a singlet state for every remotely prepared qubit. Particles 1 and 2, which Alice and Bob both share, have the following EPR states:

$$|\Psi^-\rangle_{12} = \frac{1}{\sqrt{2}}(|0\rangle_1|1\rangle_2 - |1\rangle_1|0\rangle_2) \qquad (49)$$

Alice can choose to measure particle 1 on whichever basis she likes because she is aware of the state. By projecting onto the $\{|\Psi\rangle, |\Psi_\perp\rangle\}$ basis, Alice performs the measurement on particle 1. Writing the Entangled state $|\Psi^-\rangle_{12}$ in qubit basis $\{|\Psi\rangle, |\Psi_\perp\rangle\}$

$$|\Psi^-\rangle_{12} = \frac{1}{\sqrt{2}}(|\Psi\rangle_1|\Psi_\perp\rangle_2 - |\Psi_\perp\rangle_1|\Psi\rangle_2) \qquad (50)$$

Bob's qubit will be in the desired state of $|\Psi\rangle$ if Alice's single particle Von-Neumann measurement yields the result $|\Psi_\perp\rangle$. In the event that Alice gets the result $|\Psi\rangle$, Bob's qubit will be $|\Psi_\perp\rangle$. Therefore, Bob is instructed to conduct the basis-specific NOT operation on his qubit by Alice's transmitted cbit (classical bit), which transforms Bob's qubit into $|\Psi_\perp\rangle \Longrightarrow |\Psi\rangle$.

However, due to the nonunitarity and consequent nonphysicality of a universal NOT operation (Bužek, Hillery, & Werner, 1999; Li, Luo, & Lai, 2018), Bob is unable to reliably flip his qubit when he ends up with $|\Psi_\perp\rangle$ if Alice intends to remotely prepare an arbitrary pure qubit, not from a prespecified great circle. As a result, the protocol is nondeterministic and only has a 50% chance of success for each given qubit.

For qubit chosen from polar Great circle, i.e., Φ, is zero.

$$|\Psi\rangle = \cos\frac{\theta}{2}|0\rangle + \sin\frac{\theta}{2}|1\rangle$$

$$|\Psi_\perp\rangle = \cos\frac{\theta}{2}|1\rangle - \sin\frac{\theta}{2}|0\rangle$$

After obtaining the classical information from Alice, Bob only needs to perform a rotation (apply $i\sigma_y$) or do nothing. For a qubit selected from the Bloch sphere's equatorial line such that $\theta = \frac{\pi}{2}$,

$$|\Psi\rangle = \frac{1}{\sqrt{2}}(|0\rangle + \exp i\Phi|1\rangle)$$

$$|\Psi_\perp\rangle = \frac{1}{\sqrt{2}}(|0\rangle - \exp^{i\Phi}|1\rangle)$$

where $|\Psi\rangle$ can be obtained by applying σ_z. Thus, if Alice and Bob share a single unit of entanglement (one ebit), a qubit selected from the equatorial or polar great circles on a Bloch sphere can be remotely prepared using one classical bit (cbit). Therefore, one cbit is all that is needed to remotely prepare a real known qubit, whereas two cbits are needed to transmit an unknown qubit.

Furthermore, Alice can mimic the measurement statistics on a qubit at Bob's location using one ebit and one cbit if the goal is to simulate the measurement statistics rather than create an arbitrary qubit. The protocol is termed as remote state measurement protocol (RSM). For the general state, the classical communication cost of RSP and Teleportation would be equal according to Lo's Conjecture (Lo, 2000), which was proved later (Hayashi, Hashimoto, & Horibe, 2003; Leung & Shor, 2003).

NMR devices have been used to implement the first RSP and RSM procedures for qubits from the special ensembles (polar and equatorial) spanning interatomic distances (Peng et al., 2003). Since then, reports have also been made about the experimental remote preparation of several kinds of constrained states. Most of the protocols used among them allowed for the construction of arbitrary pure states with a 50% success probability. Two RSP schemes were proposed with spontaneous parametric downconversion, Xiang, Li, Yu, and Guo (2005) and Peters, Barreiro, Goggin, Wei, and Kwiat (2005). By utilizing a partial polarizer to apply a generalized polarization measurement to one photon of a polarization-entangled pair produced by a BBO sandwich crystal (schematically shown in Fig. 21), Peter et al. remotely manufactured single photons in arbitrary polarization qubits. With a typical fidelity above 99.54%, they were able to create 18 arbitrary states with varying degrees of mixedness or purity over (and within) the whole Poincare sphere.

In 2010, wu et al. (2010) and Killoran, Biggerstaff, Kaltenbaek, Resch, and Lütkenhaus (2010) presented an experimental implementation of a fully deterministic RSP protocol that allowed the preparation of 18 arbitrary (6 mixed and 12 pure) qubit states with an average fidelity of 0.9947 and 178 arbitrary (mixed and pure) qubit states with an average fidelity of 0.995, respectively, where entangled photons are prepared via SPDC in a nonseparable polarization state. Alshowkan et al. (2021) have remotely prepared quantum states between each pair of nodes in a three-node optical fiber network by successfully distributing polarization-entangled photons. The source node where the entangled photons are generated is approximately 1.2 km and 250 m apart from the other two nodes. Remote State
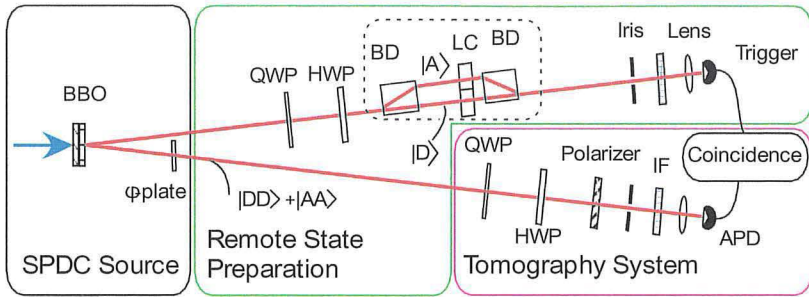
Fig. 21 Experimental schematics for Remote state preparation. *HWP*, half-wave plate; *QWP*, quarter-wave plate; *BD*, beam displacer; *LC*, liquid crystal. By evenly pumping two BBO crystals in a two-crystal geometry (with their optic axes in perpendicular planes and the relative phase adjusted by tilting an HWP (ϕ-plate) around its vertical optic axis), the entangled state $|DD\rangle + |AA\rangle / \sqrt{2}$ is produced. A QWP and an HWP are then placed in front of a partial polarizer made by LC and BD, as illustrated in the *dashed box*, to project the trigger photon into an arbitrary polarization state partially. The sister photon is produced into the desired state based on the detection of this photon. *Adapted with permission from Peters, N. A., Barreiro, J. T., Goggin, M. E., Wei, T.-C., & Kwiat, P. G. (2005). Remote state preparation: Arbitrary remote control of photon polarization. Physical Review Letters, 94(15), 150502.*

Preparation protocol has been performed using spin states of individual electrons in quantum dots, but the photons emitted by them are yet to enter this league (Xia, Lu, Song, & Song, 2010).

6.4 Quantum computing

Quantum Computation refers to the large-scale coherent processing of information via quantum systems. This field has generated tremendous interest and research over the last few decades with several architectures, primarily based on two-dimensional systems called quantum bits or "qubits." The most popular platforms among these are superconducting qubits, those based on semiconductor heterostructures, ion traps, color vacancies in diamonds, NMR quantum processors, as well as photonic platforms. In this section, we look at the evolution of photonic quantum information processing, both toward gate-based quantum computing applications and the applications based on BosonSampling problems, which are specifically aimed at demonstrating quantum supremacy.

If we consider photons as particles, information can be encoded onto some bipartite degree of freedom of individual photons, like polarization. Such an encoding requires two distinct optical modes to be present, which is referred to as "dual-rail encodings" (Knill, Laflamme, & Milburn, 2001).
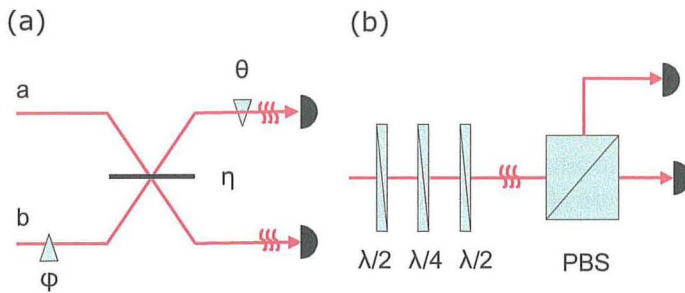
(a)   (b)

Fig. 22 Dual-rail qubit manipulation and detection. (A) A spatial dual-rail qubit evolving into any single qubit using the beamsplitter and phase-shifter circuit. Measurement of the spatial mode that holds the photons projects it in the computational basis. (B) On a polarization dual-rail qubit, random single-qubit evolution is produced by combining half- and quarter-wave plates maintained at specific angles. On a computational basis, the qubits are located using a polarizing beamsplitter (PBS) and photon counting module. *Adapted with permission from Ralph, T. C., & Pryde, G. J. (2010). Optical quantum computation. In Progress in optics (Vol. 54, pp. 209–269). Elsevier.*

Fig. 22 illustrates simplistic ways of achieving such encodings in terms of orthogonal optical modes. Considering two identical Spatiotemporal modes and populating either of the modes with a single photon, one can define the logical qubits $|0\rangle$ and $|1\rangle$. Further, using a beamsplitter and phase shifters, single–qubit operations can be achieved. In a very similar fashion, using waveplates/retarders and polarizing beamsplitters, the polarization encoding can be converted to dual–rail spatial encoding.

In discussing gate–based quantum computing, the concept of universal quantum gate sets emerges. This is a set of gates that enables any n–qubit unitary transformation to be implemented to arbitrary accuracy for any n (Nielsen & Chuang, 2002). A sufficient universal set of gates comprises arbitrary single–qubit unitary operations as well as a maximally entangling two–qubit gate. A popular example of a two–qubit gate is the Controlled–NOT (CNOT) gate. A closely related maximally entangling two–qubit gate is the Controlled–Sign gate (CZ). A CZ gate can be transformed into a CNOT gate by placing Hadamard gates before and after the CZ gate on the target qubit.

Arbitrary single qubit unitaries require simple linear interactions and are relatively straightforward in dual–rail schemes. However, the fact that photons are chargeless, massless, and in principle not interactive with each other causes a challenge toward implementing two- or multiqubit gates. One solution is to use a χ^3 nonlinear medium to induce a cross–Kerr effect between two–photon modes as first proposed by Milburn (1989). While this was

attempted, there are many difficulties with this approach of using in-line nonlinear interactions. Linear optics would be a more efficient route, and one of the early works toward this direction was the seminal work by Reck, Zeilinger, Bernstein, and Bertani (1994), which proved that using linear optics and a single photon, any quantum unitary could be simulated. However, the use of unitary coding causes this scheme to have an exponential overhead making its usage limited in quantum computation. Then came the breakthrough work from Knill et al. (2001). Popularly known as the KLM scheme, the work showed how one could generate a scalable linear optics scheme for quantum computing. While they also used dual-rail encoding, arbitrary processing was predicted to be possible without in-line nonlinearity or an exponential overhead. The KLM toolbox comprises the following requirements: single-photon sources, photon-counting detectors, and electro-optic feedforward (Ralph & Pryde, 2010). KLM essentially utilizes a trade-off between in-line nonlinearities and off-line (measurement-induced) nonlinearities. The KLM protocol led to a huge surge of research activity in dual-rail linear optical schemes, thus heralding the onset of a whole new field called "linear optical quantum computing (LOQC)" (Kok et al., 2007).

LOQC implicitly assumes the circuit model of quantum computation. Raussendorf and Briegel (2001) have suggested an alternative way of performing quantum computing which is called cluster-state quantum computation. The methodology is based on measurement-induced quantum evolution and is sometimes called "one-way" quantum computation. The cluster-state approach is particularly compatible with the emphasis in many optical quantum computation architectures on measurement-induced nonlinearities and offline resources.

When one thinks of the choice of degree of freedom of a single photon for performing quantum computing, many contenders exist, like path, frequency, time-bin, and polarization encodings. Orthogonal polarization states of the photon's electric field offer themselves as a natural practical choice for photonic qubits. Both these logical modes are degenerate and copropagating, thus rendering most sources of phase noise in an optical circuit as a common mode. This makes the qubit robust against dephasing.

Linear optical transformations have been performed on a single qubit, for instance, by Peters, Altepeter, Jeffrey, Branning, and Kwiat (2005). The choice of a single-photon source for most demonstrations of single-qubit operations has been spontaneous parametric downconversion. In SPDC sources, as discussed above, the photons are generated as pairs of photons.

Thus, if we postselect only those events from the detection record in which two photons are detected simultaneously or in coincidence (within a preset narrow time window called coincidence time window), we only record the part of the state which is due to pairs of photons. Thus, combining SPDC, the polarization degree of freedom, and postselection, one can perform two-qubit experiments. However, scalability remains a concern as the inherently probabilistic nature of the process makes this not intrinsically scalable to large-scale quantum information processing.

Ralph, Langford, Bell, and White (2002) and independently Hofmann and Takeuchi (2002) proposed a simplification of the KLM scheme (and many such modifications of the KLM scheme have been proposed in several works that followed) that could provide a powerful proof of principle of measurement-induced nonlinearity gates without the attendant architectural overheads. Using SPDC sources and several improvements in circuit design, entangling gate fidelities of up to 0.98 have been achieved (Lanyon et al., 2009).

A variety of gates and protocols have been demonstrated toward LOQC, thus proving that optics is a suitable technology for performing QIP applications. The outstanding challenge is toward scalability both in terms of resource usage to overcome nondeterminism and to obtain fault tolerance. The original KLM proposal for LOQC requires an ideal single-photon source, a device that, when triggered, produces one and only one photon into a desired mode with unit efficiency. Deterministic photon sources based on quantum dots as well as color centers in diamonds are a natural step toward such requirements (Pezzagna & Meijer, 2021; Prawer & Greentree, 2008; Sparavigna, 2022). Another important requirement for scalability would be to reduce the size of the overall experiment. Free space optics may not be the right path forward toward this. Instead, one can think of hardwired optical circuits on the micro-scale using some form of integrated optics (Arrazola et al., 2021; Chi et al., 2022). While they would naturally be beneficial vis-à-vis size and stability, such circuits should also simplify mode-matching operations that are key to achieving high-quality classical and nonclassical interference. The O'Brien group has many demonstrations in this domain, including nondeterministic C-NOT gates (Politi, Cryan, Rarity, Yu, & O'Brien, 2008) and integrated C-NOT gate for polarization qubits (Sparrow et al., 2019).

Now, we are going to shift gears from gate-based universal quantum computing to a different class of problems that are also aimed at demonstrating quantum primacy/supremacy/advantage. Quantum primacy/supremacy/advantage is the goal of showing that a programmable quantum computer solves a computational problem that is currently infeasible for

nonquantum or "classical" computers (Durham, Garisto, & Wiesner, 2021; Preskill, 2019). Several interesting intermediate models of quantum computation have been proposed. These models do not enable universal quantum computation, but still provide a dramatic increase in computational speed for particular tasks. In contrast to the KLM scheme discussed above, these models need neither entangling gate operations, adaptive measurements, nor ancilla photons and are thus technically more feasible. In a major breakthrough, Aaronson and Arkhipov (2010) argued that efficient classical simulation of linear optical systems was not possible, even if that simulation was only required to be accurate to within a reasonable total variation distance. Their argument revealed a deep connection between the complexity of sampling from quantum computers and conjectures regarding the average-case complexity of a range of combinatorial problems. The linear optical system they proposed was the class of problems called BosonSampling, which is the production of samples from Fock basis measurements of linearly scattering individual bosons. Using the current state of the art of classical computation, an implementation of BosonSampling using 50 photons would be sufficient to demonstrate quantum supremacy (Lund, Bremner, & Ralph, 2017).

Since then, Aaronson and Arkhipov's BosonSampling problem has seen implementation attempts by many experimental teams. The initial demonstrations used single photons based on SPDC, for instance (Tillmann et al., 2013). SPDC is an inherently probabilistic process and strongly reduces emission probabilities. BosonSampling with a "true" single-photon input was thus the next requirement. In Loredo et al. (2017) Andrew White's group at the University of Queensland reported a BosonSampling device that operated with a bright solid-state source of single-photon Fock states with high photon-number purity: the emission from an efficient and deterministic quantum dot-micropillar system is demultiplexed into three partially indistinguishable single photons, with a single-photon purity of 0.990 ± 0.001, interfering in a linear optics network. The experimental setup for the same is shown in Fig. 23. As this source was found to be more efficient than SPDC ones, the BosonSampling experiment was faster than previous equivalent implementations.

Almost in parallel, during the same year, the Pan group from USTC China reported another BosonSampling experiment (Wang et al., 2017). They also used actively demultiplexed single-photon sources based on a quantum dot-micropillar with simultaneously high efficiency, purity, and indistinguishability. In addition, they also developed robust multiphoton interferometers with a 99% transmission rate. They implemented and
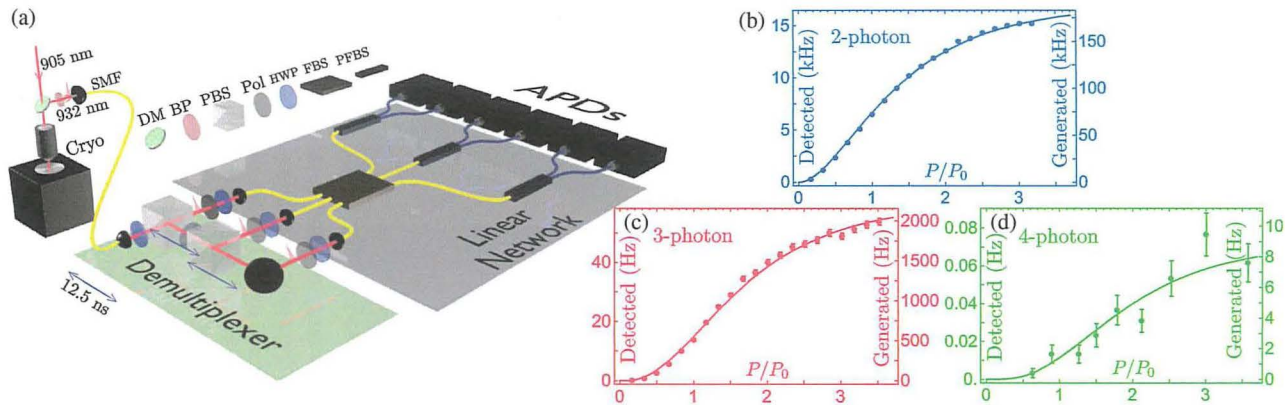
Fig. 23 Experimental schematic of the BosonSampling device reported by Andrew White's group. (A) After being filtered by a dichroic mirror (DM) and a 0.85 nm FWHM bandpass filter (BP), single-photon emission at 932 nm from the 905 nm excitation laser is subsequently collected by a single-mode fiber (SMF). At the input of the BosonSampling circuit, a passive demultiplexer with variable transmittances—half-wave plates (HWP) and polarizing beamsplitters (PBS)—and compensating delay lines of 12.5 ns probabilistically split three consecutive single photons into different spatial modes. A 3×3 nonpolarizing fiber beamsplitter (FBS), a 6×6 polarizing fiber beamsplitter (PFBS), half-wave plates, and polarizers are some of the linear components that make up the 6×6 network. Two- and threefold correlation measurements are recorded using six APDs to sample from the BosonSampling device's output distribution. (B–D) Taken directly from the demultiplexed source, 2,3,4-photon rates were detected and created. For the source modulo detector efficiencies, typically 30% for the used APDs, a factor of $(1/0.3)^n$ is included in the computed rates. A second tunable beamsplitter is used to get the four-photon count rates from the demultiplexer in (A). Curves are fitted to $c_{(max)}^n (1 - e^{(-P/P_0)})^n$, where $c_{(max)}^{(2)} = 186.4 kHz$, $c_{(max)}^{(3)} = 2202 Hz$, and $c_{(max)}^{(4)} = 8.8 Hz$ denote maximal n-photon produced rates. Adapted with permission from Loredo, J. C., Broome, M. A., Hilaire, P., Gazzano, O., Sagnes, I., Lemaitre, A., …White, A. G. (2017). Boson sampling with single-photon Fock states from a bright solid-state source. Physical Review Letters, 118(13), 130503. https://doi.org/10.1103/PhysRevLett.118.130503.

validated three-, four-, and five-photon BosonSampling and achieved sampling rates of 4.96 kHz, 151 Hz, and 4 Hz, respectively, which were over 24,000 times faster than previous experiments.

In the experiments so far, the full output photon distribution was easily calculated and could be completely verified with even the earliest classical computers. Thus, they were more proof of principle and did not really aim at demonstrating quantum supremacy. For this, one needs multiphoton BosonSampling machines with increasingly larger photon and mode numbers and faster sampling rates. For a boson sampler that is large enough to demonstrate a quantum advantage, the possible number of outputs will be large enough that the output samples will be sparse, i.e., each output will be observed only once in any reasonable experiment. The 2019 work from the Pan group (Wang et al., 2019) was the first step toward such an aim. Here, they performed experiments with 20 pure single photons and fed them into a 60-mode interferometer. The schematic is shown in Fig. 24. In the output, they detected up to 14 photons and sampled over Hilbert spaces with a size up to 3.7×10^{14}, over 10 orders of magnitude larger than all previous experiments. This thus enabled the first genuine sampling regime where it became impossible to exhaust all possible output combinations. The results
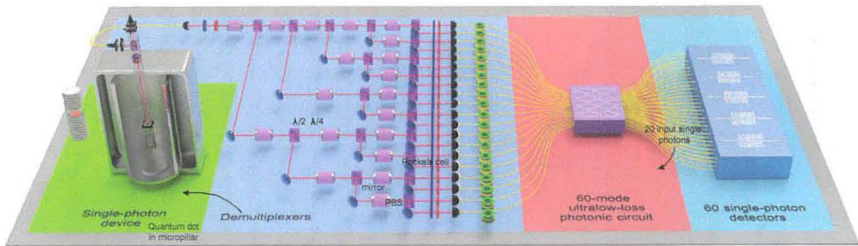

Fig. 24 A single *InAs–GaAs* quantum dot resonantly coupled to a microcavity in an experimental BosonSampling setup emits pulsing resonance fluorescence single photons. The stream of photon pulses is demultiplexed using 19 pairs of Pockels cells (PCs) and polarizing beamsplitters (PBSs), which convert the stream into 20 different spatial modes. Time delays are adjusted using optical fibers with different lengths. The 3D integrated, 60-mode, ultralow-loss photonic circuit, which consists of 396 beamsplitters and 108 mirrors, is fed with these 20 input single photons. Sixty superconducting nanowire single-photon detectors (with quantum efficiencies ranging from 0.6 to 0.82) next detect the output single photons, and a 64-channel coincidence count unit records coincidences. *Adapted with permission from Wang, H., Qin, J., Ding, X., Chen, M.-C., Chen, S., You, X., ...Pan, J.-W. (2019). Boson sampling with 20 input photons and a 60-mode interferometer in a 1 0 14-dimensional Hilbert space. Physical Review Letters, 123(25), 250503.*

were validated against distinguishable samplers and uniform samplers with a confidence level of 99.9%.

The original BosonSampling problem involved constructing a many-channel interferometer and injecting either one photon or zero photons into each input port. After this, signals would be characterized via a multiphoton coincidence measurement at the output ports of a multichannel interferometer, which enacts a random signal transformation. The BosonSampling analysis shows that subject to clear and plausible assumptions and conditions, the problem of sampling the circuit output is hard for classical machines but can be efficiently executed through quantum photonic interferometry (Sanders, 2021). The ideal formulation is difficult to realize experimentally, so BosonSampling has been further generalized, for instance, to Gaussian boson sampling (Hamilton et al., 2017). While proofs of computational primacy are harder to obtain in the case of Gaussian boson sampling, the community focused on "spoofing" the quantum results, which means devising classical algorithms that would succeed in simulating the quantum results and thereby negating the quantum primacy claim.

Significantly increasing the size of the quantum sampling problem is one way of keeping the quantum sampling experiment well ahead of classical spoofing. This has been the focus of the most recent experiments in this genre, both demonstrating Gaussian boson sampling (GBS). In the first experiment in 2020 (Zhong et al., 2020), the Pan group performed Gaussian boson sampling by sending 50 indistinguishable single-mode squeezed states into a 1-mode ultralow-loss interferometer with full connectivity and random matrix–the whole optical setup is phase-locked, and the output was sampled using 100 high-efficiency single-photon detectors. The obtained samples are validated against plausible hypotheses exploiting thermal states, distinguishable photons, and uniform distribution. The photonic quantum computer generated up to 76 output photon clicks, which yielded an output state-space dimension of 10^{30} and a sampling rate that is 10^{14} faster than using the state-of-the-art simulation strategy and supercomputers. Instead of using single photons, GBS fully utilizes the Gaussian nature of the PDC sources and utilizes single-mode squeezed states (SMSS) as input nonclassical light sources, which be deterministically prepared. The group named their GBS machine *Jiuzhang*.

The USTC group went on to then create yet another photonic quantum computer, *Jiuzhang 2.0*. In 2021 (Zhong et al., 2021), the group reported phase-programmable GBS which produced up to 113 photon detection events out of a 144-mode photonic circuit which is shown in Fig. 25.
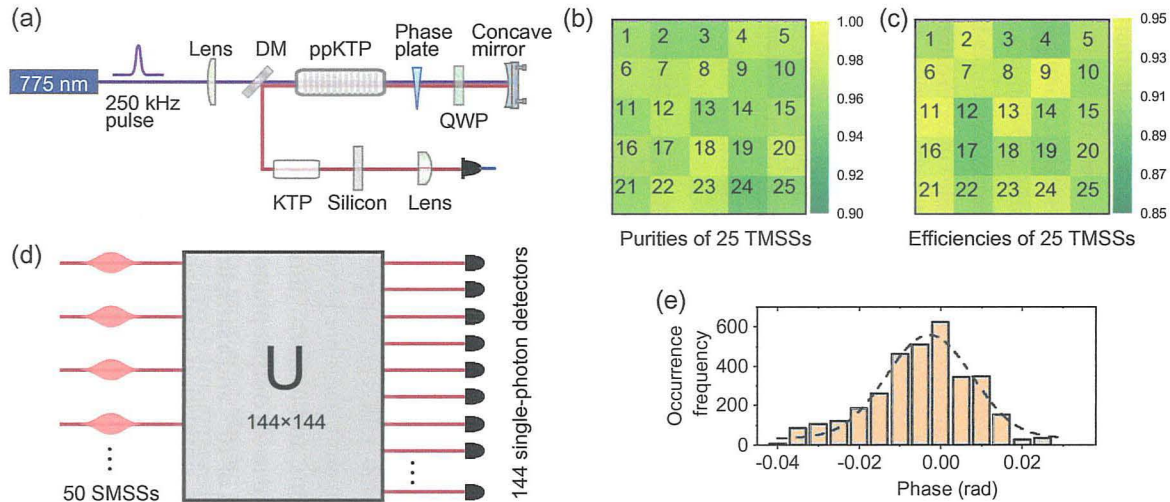
Fig. 25 (A) The experimental schematic for amplifying squeezed light by stimulated parametric downconversion. To induce emission, the downconverted photons are polarization exchanged, and their relative phase with pump light is controlled by the QWP and the wedge phase plate. The pump and parametric photons are focused by the concave mirror back to the PPKTP. Before entering the single-mode fiber, the remaining pumping light is filtered away using an antireflection-coated silicon plate. The squeezed light is then transmitted via a KTP crystal for birefringence compensation. (B) Photon indistinguishability, which may alternatively be expressed as the overlap of the wave functions of two independent photons, is the definition of the purity of an entangled source. Here, it is demonstrated that the 25 squeezed light sources' average purities are 0.961. (C) The ratio of produced photons collected in the single-mode fiber is known as the collection efficiency. The average collecting efficiency for the aforementioned 25 squeezed light sources is 0.918. (D) An overview of the GBS setup, which involves sending 25 pairs of two-mode squeezed photons into a 144-mode interferometer and using 144 single-photon detectors to read out the output distribution. (E) The setup's phase fluctuations, as depicted in the histogram, are within 0.06 rad per hour. *Adapted with permission from Zhong, H.-S., Deng, Y.-H., Qin, J., Wang, H., Chen, M.-C., Peng, L.-C., …Pan, J.-W. (2021). Phase-programmable gaussian boson sampling using stimulated squeezed light. Physical Review Letters, 127(18), 180502. https://doi.org/10.1103/PhysRevLett.127.180502.*

For this, they developed a new high-brightness and scalable quantum light source, exploring the idea of stimulated emission of squeezed photons, which simultaneously had near-unity purity and efficiency. They showed that their GBS experiment passed a nonclassicality test based on inequality constraints, and genuine higher-order correlations were revealed in the GBS samples as evidence of robustness against possible classical simulation schemes. *Jiuzhang 2.0* yielded a Hilbert space dimension up to 10^{43} and a sampling rate 10^{24} faster than using brute-force simulation on classical computers.

Deshpande et al. (2022) proposed quantum computational advantage architecture for high-dimensional GBS using a programmable photonic processor in January 2022. Later on, in June 2022, the Canadian company, Xanadu launched the world's first photonic processor *Borealis*, which offered programmability on all its gates. It carried out GBS on 216 squeezed states entangled with three-dimensional connectivity in merely 36 μs, which would otherwise take more than 9000 years on a supercomputer (Madsen et al., 2022).

These recent experiments represent rapid advancement in experimental quantum sampling, making classical spoofing of such demonstrations less plausible and establishing more firmly that we are indeed in an age of quantum primacy for computing. The question now arises as to whether these quantum samplers can solve useful computational problems. There are claims that such samplers can tackle meaningful problems in quantum chemistry as well as random number generators, but there is, as of now, no convincing experimental demonstration of such claims.
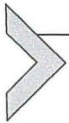
7. Conclusion and outlook

In this chapter, different architectures for generating single and entangled photons have been discussed. These include both probabilistic and deterministic/on-demand photon sources. In the first part of the chapter, we have discussed the underlying physics of these photon sources and details regarding the generation mechanisms. In the second part, applications of photons in quantum technologies have been highlighted. The main applications that we focused on are quantum communications, including quantum key distribution, remote state preparation, and quantum teleportation as well as quantum computing (both gate-based and BosonSampling). We find that photonic quantum science and technologies have seen significant advances over the last few decades. While on one hand, there is a concerted effort toward making photon sources that generate photons with ideal

characteristics, on the other hand, the usage of photons in several quantum technology applications has also seen progress in leaps and bounds. While photons remain the natural choice in quantum communication experiments, recent advances in photonic quantum computing make it a strong contender for emerging as the "ultimate" choice of quantum computing architecture. The Nobel Prize in Physics 2022 being awarded to photonic quantum information efforts has provided renewed impetus to the field of photonic quantum science and technologies, and we are poised to witness further breakthroughs in this domain in the years to come.

Acknowledgments

References

Aaronson, S., & Arkhipov, A. (2010). The computational complexity of linear optics. *arXiv*. https://doi.org/10.48550/ARXIV.1011.3245.

Agrawal, G. P. (2013). *Vol. 19892. Nonlinear fiber optics* (5th ed.). New York: Academic Press. 44 p.

Alléaume, R., Treussart, F., Messin, G., Dumeige, Y., Roch, J.-F., Beveratos, A., … Grangier, P. (2004). Experimental open-air quantum key distribution with a single-photon source. *New Journal of Physics*, 6(1), 92.

Alshowkan, M., Williams, B. P., Evans, P. G., Rao, N. S. V., Simmerman, E. M., Lu, H.-H., … Lukens, J. M. (2021). Reconfigurable quantum local area network over deployed fiber. *PRX Quantum*, 2(4), 040304.

Andersen, S. K. H., Kumar, S., & Bozhevolnyi, S. I. (2017a). Ultrabright linearly polarized photon generation from a nitrogen vacancy center in a nanocube dimer antenna. *Nano Letters*, 17(6), 3889–3895. https://doi.org/10.1021/acs.nanolett.7b01436. PMID: 28471666.

Andersen, S. K. H., Kumar, S., & Bozhevolnyi, S. I. (2017b). Ultrabright linearly polarized photon generation from a nitrogen vacancy center in a nanocube dimer antenna. *Nano Letters*, 17(6), 3889–3895. https://doi.org/10.1021/acs.nanolett.7b01436.

Anderson, M., Müller, T., Huwer, J., Skiba-Szymanska, J., Krysa, A. B., Stevenson, R. M., … Shields, A. J. (2020). Quantum teleportation using highly coherent emission from telecom C-band quantum dots. *npj Quantum Information*, 6(1), 14. https://doi.org/10.1038/s41534-020-0249-5.

Anderson, M., Müller, T., Skiba-Szymanska, J., Krysa, A. B., Huwer, J., Stevenson, R. M., … Shields, A. J. (2021). Coherence in single photon emission from droplet epitaxy and Stranski–Krastanov quantum dots in the telecom C-band. *Applied Physics Letters*, 118(1), 014003. https://doi.org/10.1063/5.0032128.

Arrazola, J. M., Bergholm, V., Brádler, K., Bromley, T. R., Collins, M. J., Dhand, I., … Zhang, Y. (2021). Quantum circuits with many photons on a programmable nano-photonic chip. *Nature*, 591(7848), 54–60. https://doi.org/10.1038/s41586-021-03202-1.

Ashcroft, N. W., & Mermin, N. D. (2022). *Solid state physics*. Cengage Learning.

Aspect, A., Grangier, P., & Roger, G. (1981). Experimental tests of realistic local theories via Bell's theorem. *Physical Review Letters*, 47(7), 460.

Aspect, A., Grangier, P., & Roger, G. (1982). Experimental realization of Einstein-Podolsky-Rosen-Bohm Gedankenexperiment: A new violation of Bell's inequalities. *Physical Review Letters*, 49(2), 91.

Basset, F. B., Valeri, M., Neuwirth, J., Polino, E., Rota, M. B., Poderini, D., ... Trotta, R. (2022). Daylight entanglement-based quantum key distribution with a quantum dot source. *arXiv:2206.15360*. http://arxiv.org/abs/2206.15360. 2022-10-11.

Basso Basset, F., Salusti, F., Schweickert, L., Rota, M. B., Tedeschi, D., Covre da Silva, S. F., ... Trotta, R. (2021). Quantum teleportation with imperfect quantum dots. *npj Quantum Information*, 7(1), 7. https://doi.org/10.1038/s41534-020-00356-0.

Bennett, C. H., & Brassard, G. (1989). Experimental quantum cryptography: The dawn of a new era for quantum cryptography: The experimental prototype is working. *ACM SIGACT News*, 20(4), 78–80. https://doi.org/10.1145/74074.74087.

Bennett, C. H., Brassard, G., Crépeau, C., Jozsa, R., Peres, A., & Wootters, W. K. (1993). Teleporting an unknown quantum state via dual classical and Einstein-Podolsky-Rosen channels. *Physical Review Letters*, 70(13), 1895–1899. https://doi.org/10.1103/PhysRevLett.70.1895.

Bennett, C. H., DiVincenzo, D. P., Shor, P. W., Smolin, J. A., Terhal, B. M., & Wootters, W. K. (2001). Remote state preparation. *Physical Review Letters*, 87(7), 077902. https://journals.aps.org/prl/pdf/10.1103/PhysRevLett.87.077902..

Berchera, I. R., & Degiovanni, I. P. (2019). Quantum imaging with sub-Poissonian light: Challenges and perspectives in optical metrology. *Metrologia*, 56(2), 024001.

Bernien, H., Childress, L., Robledo, L., Markham, M., Twitchen, D., & Hanson, R. (2012). Two-photon quantum interference from separate nitrogen vacancy centers in diamond. *Physical Review Letters*, 108(4), 043604. https://doi.org/10.1103/PhysRevLett.108.043604.

Beveratos, A., Brouri, R., Gacoin, T., Villing, A., Poizat, J.-P., & Grangier, P. (2002). Single photon quantum cryptography. *Physical Review Letters*, 89(18), 187901. https://doi.org/10.1103/PhysRevLett.89.187901.

Borah, D. J., Mostako, A. T. T., Borgogoi, A. T., Saikia, P. K., & Malakar, A. (2020). Modified top-down approach for synthesis of molybdenum oxide quantum dots: Sonication induced chemical etching of thin films. *RSC Advances*, 10(6), 3105–3114. https://doi.org/10.1039/C9RA09773B.

Bouwmeester, D., Pan, J.-W., Mattle, K., Eibl, M., Weinfurter, H., & Zeilinger, A. (1997). *Nature*, 390(6660), 575–579. https://doi.org/10.1038/37539.

Boyd, R. W. (2020). *Nonlinear optics*. Academic Press.

Briegel, H.-J., Dür, W., Cirac, J. I., & Zoller, P. (1998). Quantum repeaters: The role of imperfect local operations in quantum communication. *Physical Review Letters*, 81(26), 5932.

Bužek, V., Hillery, M., & Werner, R. F. (1999). Optimal manipulations with qubits: Universal-not gate. *Physical Review A*, 60(4), R2626. https://journals.aps.org/pra/pdf/10.1103/PhysRevA.60.R2626..

Cao, Y., Li, Y.-H., Zou, W.-J., Li, Z.-P., Shen, Q., Liao, S.-K., ... Pan, J.-W. (2018). Bell test over extremely high-loss channels: Towards distributing entangled photon pairs between earth and the moon. *Physical Review Letters*, 120(14), 140405.

Castelletto, S., & Boretti, A. (2020). Silicon carbide color centers for quantum applications. *Journal of Physics: Photonics*, 2(2), 022001.

Chatterjee, R., Joarder, K., Chatterjee, S., Sanders, B. C., & Sinha, U. (2020). qkdSim, a simulation toolkit for quantum key distribution including imperfections: Performance analysis and demonstration of the B92 protocol using heralded photons. *Physical Review Applied*, 14(2), 024036. https://doi.org/10.1103/PhysRevApplied.14.024036.

Chen, J., Ma, Q., Wu, X.-J., Li, L., Liu, J., & Zhang, H. (2019). Wet-chemical synthesis and applications of semiconductor nanomaterial-based epitaxial heterostructures. *Nano-Micro Letters*, 11, 86. https://doi.org/10.1007/s40820-019-0317-6.

Chen, Y., Zopf, M., Keil, R., Ding, F., & Schmidt, O. G. (2018). Highly-efficient extraction of entangled photons from quantum dots using a broadband optical antenna. *Nature Communications*, 9(1), 1–7.

Chi, Y., Huang, J., Zhang, Z., Mao, J., Zhou, Z., Chen, X., ... Wang, J. (2022). *Nature Communications*, *13*(1), 1166. https://doi.org/10.1038/s41467-022-28767-x.

Clapp, A. R., Medintz, I. L., Mauro, J. M., Fisher, B. R., Bawendi, M. G., & Mattoussi, H. (2004). Fluorescence resonance energy transfer between quantum dot donors and dye-labeled protein acceptors. *Journal of the American Chemical Society*, *126*(1), 301–310.

Clauser, J. F., & Shimony, A. (1978). Bell's theorem. Experimental tests and implications. *Reports on Progress in Physics*, *41*(12), 1881.

Couteau, C. (2018). Spontaneous parametric down-conversion. *Contemporary Physics*, *59*(3), 291–304. https://doi.org/10.1080/00107514.2018.1488463.

Davies, G., Hamer, M. F., & Price, W. C. (1976). Optical studies of the 1.945 eV vibronic band in diamond. *Proceedings of the Royal Society of London. A. Mathematical and Physical Sciences*, *348*(1653), 285–298. https://doi.org/10.1098/rspa.1976.0039.

de Brito, D. B., & Ramos, R. V. (2010). Analysis of heralded single-photon source using four-wave mixing in optical fibers via Wigner function and its use in quantum key distribution. *IEEE Journal of Quantum Electronics*, *46*(5), 721–727. https://doi.org/10.1109/JQE.2009.2034390.

Deshpande, A., Mehta, A., Vincent, T., Quesada, N., Hinsche, M., Ioannou, M., ... Dhand, I. (2022). Quantum computational advantage via high-dimensional gaussian boson sampling. *Science Advances*, *8*(1), eabi7894. https://doi.org/10.1126/sciadv.abi7894.

Díaz-González, M., de la Escosura-Muñiz, A., Fernandez-Argüelles, M. T., Alonso, F. J. G., & Costa-Fernandez, J. M. (2020). Quantum dot bioconjugates for diagnostic applications. In *Surface-modified nanobiomaterials for electrochemical and biomedicine applications* (pp. 133–176). Springer.

Domínguez-Serna, F. A., Rojas, F., & Garay-Palmett, K. (2020). Quantum teleportation with hybrid entangled resources prepared from heralded quantum states. *Journal of the Optical Society of America B*, *37*(3), 695–701. https://doi.org/10.1364/JOSAB.377687.

Durham, I., Garisto, D., & Wiesner, K. (2021). Physicists need to be more careful with how they name things. *Scientific American*, *1*.

Dzurnak, B., Stevenson, R. M., Nilsson, J., Dynes, J. F., Yuan, Z. L., Skiba-Szymanska, J., ... Shields, A. J. (2015). Quantum key distribution with an entangled light emitting diode. *Applied Physics Letters*, *107*(26), 261101. https://doi.org/10.1063/1.4938502.

Erven, C., Couteau, C., Laflamme, R., & Weihs, G. (2008). Entangled quantum key distribution over two free-space optical links. *arXiv*. https://doi.org/10.48550/ARXIV.0807.2289. Version Number: 2.

Fedrizzi, A., Herbst, T., Poppe, A., Jennewein, T., & Zeilinger, A. (2007). A wavelength-tunable fiber-coupled source of narrowband entangled photons. *Optics Express*, *15*(23), 15377–15386.

Fiorentino, M., Spillane, S. M., Beausoleil, R. G., Roberts, T. D., Battle, P., & Munro, M. W. (2007). Spontaneous parametric down-conversion in periodically poled KTP waveguides and bulk crystals. *Optics Express*, *15*(12), 7479–7488. https://doi.org/10.1364/OE.15.007479.

Freedman, S. J., & Clauser, J. F. (1972). Experimental test of local hidden-variable theories. *Physical Review Letters*, *28*(14), 938.

Friedli, P., Sigg, H., Hinkov, B., Hugi, A., Riedi, S., Beck, M., et al. (2013). Four-wave mixing in a quantum cascade laser amplifier. *Applied Physics Letters*, *102*(22), 222104. https://doi.org/10.1063/1.4807662.

Gali, Á. (2019). Ab initio theory of the nitrogen-vacancy center in diamond. *Nanophotonics*, *8*(11), 1907–1943. https://doi.org/10.1515/nanoph-2019-0154.

Gao, W. B., Fallahi, P., Togan, E., Delteil, A., Chin, Y. S., Miguel-Sanchez, J., & Imamoğlu, A. (2013). Quantum teleportation from a propagating photon to a solid-state spin qubit. *Nature Communications*, *4*(1), 2744. https://doi.org/10.1038/ncomms3744.

Gerry, C., Knight, P., & Knight, P. L. (2005). *Introductory quantum optics*. Cambridge University Press.

Gisin, N., Ribordy, G., Tittel, W., & Zbinden, H. (2002). Quantum cryptography. *Reviews of Modern Physics*, *74*(1), 145–195. https://doi.org/10.1103/RevModPhys.74.145.

Giustina, M., Versteegh, M. A. M., Wengerowsky, S., Handsteiner, J., Hochrainer, A., Phelan, K., ... Zeilinger, A. (2015). Significant-loophole-free test of Bell's theorem with entangled photons. *Physical Review Letters*, *115*(25), 250401.

Giustina, M., Versteegh, M. A. M., Wengerowsky, S., Handsteiner, J., Hochrainer, A., Phelan, K., & Zeilinger, A. (2017). A significant-loophole-free test of Bell's theorem with entangled photons. In *Quantum information science and technology III: Vol. 10442* (pp. 19–27). SPIE.

Hamilton, C. S., Kruse, R., Sansoni, L., Barkhofen, S., Silberhorn, C., & Jex, I. (2017). Gaussian Boson sampling. *Physical Review Letters*, *119*(17), 170501. https://doi.org/10.1103/PhysRevLett.119.170501.

Hanzawa, H., Nisida, Y., & Kato, T. (1997). Measurement of decay time for the NV centre in Ib diamond with a picosecond laser pulse. *Diamond and Related Materials*, *6*(11), 1595–1598. https://doi.org/10.1016/S0925-9635(97)00037-X.

Hayashi, A., Hashimoto, T., & Horibe, M. (2003). Remote state preparation without oblivious conditions. *Physical Review A*, *67*(5), 052302.

Heindel, T., Kessler, C. A., Rau, M., Schneider, C., Fürst, M., Hargart, F., ... Forchel, A. (2012). Quantum key distribution using quantum dot single-photon emitting diodes in the red and near infrared spectral range. *New Journal of Physics*, *14*(8), 083001. https://doi.org/10.1088/1367-2630/14/8/083001.

Hodgson, P. D., Bentley, M., Delli, E., Beanland, R., Wagener, M. C., Botha, J. R., & Carrington, P. J. (2018). Optical and structural properties of InGaSb/GaAs quantum dots grown by molecular beam epitaxy. *Semiconductor Science and Technology*, *33*(12), 125021. https://doi.org/10.1088/1361-6641/aae627.

Hofmann, H. F., & Takeuchi, S. (2002). Quantum phase gate for photonic qubits using only beam splitters and postselection. *Phys. Rev. A*, *66*(2), 024308. https://doi.org/10.1103/PhysRevA.66.024308.

Hong, C. K., Ou, Z. Y., & Mandel, L. (1987). Measurement of subpicosecond time intervals between two photons by interference. *Physical Review Letters*, *59*(18), 2044–2046. https://doi.org/10.1103/PhysRevLett.59.2044.

Horowicz, R., Pinard, M., & Reynaud, S. (1987). Generation of twin photon beams through intracavity four-wave mixing. *Optics Communications*, *61*(2), 142–146.

Humphreys, P. C., Kalb, N., Morits, J. P. J., Schouten, R. N., Vermeulen, R. F. L., Twitchen, D. J., ... Hanson, R. (2018). Publisher correction: Deterministic delivery of remote entanglement on a quantum network. *Nature*, *562*(7725). https://doi.org/10.1038/s41586-018-0314-9. E2–E2.

Hwa, K.-Y., Ganguly, A., Santhan, A., & Sharma, T. S. K. (2022). Synthesis of water-soluble cadmium selenide/zinc sulfide quantum dots on functionalized multiwalled carbon nanotubes for efficient covalent synergism in determining environmental hazardous phenolic compounds. *ACS Sustainable Chemistry & Engineering*, *10*(3), 1298–1315. https://doi.org/10.1021/acssuschemeng.1c07690.

Inoue, K., Waks, E., & Yamamoto, Y. (2002). Differential phase shift quantum key distribution. *Physical Review Letters*, *89*(3), 037902.

Intallura, P. M., Ward, M. B., Karimov, O. Z., Yuan, Z. L., See, P., Shields, A. J., ... Ritchie, D. A. (2007). Quantum key distribution using a triggered quantum dot source emitting near 1.3μm. *Applied Physics Letters*, *91*(16), 161103. https://doi.org/10.1063/1.2799756.

Jennewein, T., Simon, C., Weihs, G., Weinfurter, H., & Zeilinger, A. (2000). Quantum cryptography with entangled photons. *Physical Review Letters*, *84*(20), 4729–4732. https://doi.org/10.1103/PhysRevLett.84.4729.

Jiang, W. C., Lu, X., Zhang, J., Painter, O., & Lin, Q. (2015). Silicon-chip source of bright photon pairs. *Optics Express*, *23*(16), 20884–20904. https://doi.org/10.1364/OE.23.020884.

Jin, R.-B., Takeoka, M., Takagi, U., Shimizu, R., & Sasaki, M. (2015). *Scientific Reports*, *5*(1), 9333. https://doi.org/10.1038/srep09333.

Jin, X.-M., Ren, J.-G., Yang, B., Yi, Z.-H., Zhou, F., Xu, X.-F., ... Pan, J.-W. (2010). Experimental free-space quantum teleportation. *Nature Photonics*, *4*(6), 376–381.

Kaiser, F., Issautier, A., Ngah, L. A., Aktas, D., Delord, T., & Tanzilli, S. (2014). *arXiv*. https://doi.org/10.48550/ARXIV.1412.7648. Version Number: 1.

Khramtsov, I. A., Vyshnevyy, A. A., & Fedyanin, D. Y. (2018). Enhancing the brightness of electrically driven single-photon sources using color centers in silicon carbide. *npj Quantum Information*, *4*(1), 1–8.

Killoran, N., Biggerstaff, D. N., Kaltenbaek, R., Resch, K. J., & Lütkenhaus, N. (2010). Derivation and experimental test of fidelity benchmarks for remote preparation of arbitrary qubit states. *Physical Review A*, *81*(1), 012334. https://journals.aps.org/pra/pdf/10.1103/PhysRevA.81.012334..

Kim, T., Lim, S., Yun, S., Jeong, S., Park, T., & Choi, J. (2020). Design strategy of quantum dot thin-film solar cells. *Small*, *16*(45), 2002460. https://doi.org/10.1002/smll.202002460.

Knall, E. N., Knaut, C. M., Bekenstein, R., Assumpcao, D. R., Stroganov, P. L., Gong, W., ... Lukin, M. D. (2022). Efficient source of shaped single photons based on an integrated diamond nanophotonic system. *Physical Review Letters*, *129*, 053603 (arXiv preprint:2201.02731).

Knill, E., Laflamme, R., & Milburn, G. J. (2001). A scheme for efficient quantum computation with linear optics. *Nature*, *409*(6816), 46–52. https://doi.org/10.1038/35051009.

Kok, P., Munro, W. J., Nemoto, K., Ralph, T. C., Dowling, J. P., & Milburn, G. J. (2007). Linear optical quantum computing with photonic qubits. *Rev. Mod. Phys.*, *79*(1), 135–174. https://doi.org/10.1103/RevModPhys.79.135.

Kurtsiefer, C., Mayer, S., Zarda, P., & Weinfurter, H. (2000). Stable solid-state source of single photons. *Physical Review Letters*, *85*(2), 290–293. https://doi.org/10.1103/PhysRevLett.85.290.

Lanyon, B. P., Barbieri, M., Almeida, M. P., Jennewein, T., Ralph, T. C., Resch, K. J., ... White, A. G. (2009). Simplifying quantum logic using higher-dimensional Hilbert spaces. *Nature Physics*, *5*(2), 134–140. https://doi.org/10.1038/nphys1150.

Larsson, J. A., & Delaney, P. (2008). Electronic structure of the nitrogen-vacancy center in diamond from first-principles theory. *Physical Review B*, *77*(16), 165201. https://doi.org/10.1103/PhysRevB.77.165201.

Lee, D., Kim, I., & Lee, K. J. (2021). Investigation of 1064-nm pumped type II SPDC in potassium niobate for generation of high spectral purity photon pairs. *Crystals*, *11*(6), 599.

Leifgen, M., Schröder, T., Gädeke, F., Riemann, R., Métillon, V., Neu, E., ... Benson, O. (2014). Evaluation of nitrogen- and silicon-vacancy defect centres as single photon sources in quantum key distribution. *New Journal of Physics*, *16*(2), 023021. https://doi.org/10.1088/1367-2630/16/2/023021.

Leung, D. W., & Shor, P. W. (2003). Oblivious remote state preparation. *Physical Review Letters*, *90*(12), 127905.

Li, H.-R., Luo, M.-X., & Lai, H. (2018). Generalized quantum no-go theorems of pure states. *Quantum Information Processing*, *17*(7), 1–18. https://link.springer.com/content/pdf/10.1007/s11128-018-1936-4.pdf..

Liao, S.-K., Cai, W.-Q., Liu, W.-Y., Zhang, L., Li, Y., Ren, J.-G., ... Pan, J.-W. (2017). Satellite-to-ground quantum key distribution. *Nature*, *549*(7670), 43–47. https://doi.org/10.1038/nature23655.

Liñares, J., Prieto-Blanco, X., Balado, D., & Carral, G. M. (2021). Fully autocompensating high-dimensional quantum cryptography by quantum degenerate four-wave mixing. *Physical Review A*, *103*(4), 043710. https://doi.org/10.1103/PhysRevA.103.043710.

Ling, A., Peloso, M., Marcikic, I., Lamas-Linares, A., & Kurtsiefer, C. (2008). Experimental E91 quantum key distribution. In Z. U. Hasan, A. E. Craig, & P. R. Hemmer (Eds.), *Integrated optoelectronic devices 2008* (p. p. 69030U). https://doi.org/10.1117/12.778556.

Liu, C., Zhang, S., Zhao, L., Chen, P., Fung, C. H. F., Chau, H. F., ... Du, S. (2013). Differential-phase-shift quantum key distribution using heralded narrow-band single photons. *Optics Express*, *21*(8), 9505–9513.

Liu, J., Nie, Y., Xue, W., Wu, L., Jin, H., Jin, G., ... Fu, C. (2020). Size effects on structural and optical properties of tin oxide quantum dots with enhanced quantum confinement. *Journal of Materials Research and Technology*, *9*(4), 8020–8028. https://doi.org/10.1016/j.jmrt.2020.05.041.

Lo, H.-K. (2000). Classical-communication cost in distributed quantum-information processing: A generalization of quantum-communication complexity. *Physical Review A*, *62*(1), 012313. https://journals.aps.org/pra/pdf/10.1103/PhysRevA.62.012313..

Lohrmann, A., Iwamoto, N., Bodrog, Z., Castelletto, S., Ohshima, T., Karle, T. J., ... Johnson, B. C. (2015). Single-photon emitting diode in silicon carbide. *Nature Communications*, *6*(1), 1–7.

Lo Piparo, N., Razavi, M., & Munro, W. J. (2017). Measurement-device-independent quantum key distribution with nitrogen vacancy centers in diamond. *Physical Review A*, *95*(2), 022338. https://doi.org/10.1103/PhysRevA.95.022338.

Loredo, J. C., Broome, M. A., Hilaire, P., Gazzano, O., Sagnes, I., Lemaitre, A., ... White, A. G. (2017). Boson sampling with single-photon Fock states from a bright solid-state source. *Physical Review Letters*, *118*(13), 130503. https://doi.org/10.1103/PhysRevLett.118.130503.

Lund, A. P., Bremner, M. J., & Ralph, T. C. (2017). Quantum sampling problems, BosonSampling and quantum supremacy. *npj Quantum Information*, *3*(1), 15. https://doi.org/10.1038/s41534-017-0018-2.

Ma, X., Li, S., Hessel, V., Lin, L., Meskers, S., & Gallucci, F. (2019). Synthesis of luminescent carbon quantum dots by microplasma process. *Chemical Engineering and Processing— Process Intensification*, *140*, 29–35. https://doi.org/10.1016/j.cep.2019.04.017.

Ma, X.-S., Herbst, T., Scheidl, T., Wang, D., Kropatschek, S., Naylor, W., ... Zeilinger, A. (2012). Quantum teleportation over 143 kilometres using active feed-forward. *Nature*, *489*(7415), 269–273. https://doi.org/10.1038/nature11472.

Madsen, L. S., Laudenbach, F., Askarani, M. F., Rortais, F., Vincent, T., Bulmer, J. F. F., ... Lavoie, J. (2022). *Nature*, *606*(7912), 75–81. https://doi.org/10.1038/s41586-022-04725-x.

Manson, N. B., Harrison, J. P., & Sellars, M. J. (2006). Nitrogen-vacancy center in diamond: Model of the electronic structure and associated dynamics. *Physical Review B*, *74*(10), 104303. https://doi.org/10.1103/PhysRevB.74.104303.

Marcikic, I., Lamas-Linares, A., & Kurtsiefer, C. (2006). Free-space quantum key distribution with entangled photons. *Applied Physics Letters*, *89*(10), 101122. https://doi.org/10.1063/1.2348775.

Martin, A., Alibart, O., De Micheli, M. P., Ostrowsky, D. B., & Tanzilli, S. (2012). A quantum relay chip based on telecommunication integrated optics technology. *New Journal of Physics*, *14*(2), 025002.

Massa, F., Moqanaki, A., Baumeler, Ä., Del Santo, F., Kettlewell, J. A., Dakić, B., & Walther, P. (2019). Experimental two-way communication with one photon. *Advanced Quantum Technologies*, *2*(11), 1900050. https://doi.org/10.1002/qute.201900050.

McMillan, A. R., Fulconis, J., Halder, M., Xiong, C., Rarity, J. G., & Wadsworth, W. J. (2009). Narrowband high-fidelity all-fibre source of heralded single photons at 1570 nm. *Optics Express*, *17*(8), 6156–6165. https://doi.org/10.1364/OE.17.006156.

Milburn, G. J. (1989). Quantum optical Fredkin gate. *Physical Review Letters*, *62*(18), 2124–2127. https://doi.org/10.1103/PhysRevLett.62.2124.

Neu, E., & Becher, C. (2014). 6—Diamond-based single-photon sources and their application in quantum key distribution. In S. Prawer, & I. Aharonovich (Eds.), *Quantum information processing with diamond* (pp. 127–159). Woodhead Publishing. https://doi.org/10.1533/9780857096685.2.127.

Nielsen, M. A., & Chuang, I. (2002). Quantum computation and quantum information. *American Journal of Physics*, *70*(5), 558–559. https://doi.org/10.1119/1.1463744.

Pati, A. K. (2000). Minimum classical bit for remote preparation and measurement of a qubit. *Physical Review A*, *63*(1), 014302. https://journals.aps.org/pra/pdf/10.1103/PhysRevA.63.014302..

Peng, X., Zhu, X., Fang, X., Feng, M., Liu, M., & Gao, K. (2003). Experimental implementation of remote state preparation by nuclear magnetic resonance. *Physics Letters A*, *306*(5–6), 271–276. https://arxiv.org/pdf/quant-ph/0202004.pdf..

Pereira, M. D. C., Becerra, F. E., Glebov, B. L., Fan, J., Nam, S. W., & Migdall, A. (2013). Demonstrating highly symmetric single-mode, single-photon heralding efficiency in spontaneous parametric downconversion. *Optics Letters*, *38*(10), 1609–1611.

Peters, N., Altepeter, J., Jeffrey, E., Branning, D., & Kwiat, P. (2005). Precise creation, characterization, and manipulation of single optical qubits. *arXiv preprint quant-ph/0502177*.

Peters, N. A., Barreiro, J. T., Goggin, M. E., Wei, T.-C., & Kwiat, P. G. (2005). Remote state preparation: Arbitrary remote control of photon polarization. *Physical Review Letters*, *94*(15), 150502.

Petrov, N. L., Fedotov, A. B., & Zheltikov, A. M. (2019). High-brightness photon pairs and strongly antibunching heralded single photons from a highly nonlinear optical fiber. *Optics Communications*, *450*, 304–307. https://doi.org/10.1016/j.optcom.2019.04.084.

Pezzagna, S., & Meijer, J. (2021). Quantum computer based on color centers in diamond. *Applied Physics Reviews*, *8*(1), 011308. https://doi.org/10.1063/5.0007444.

Pfaff, W., Hensen, B. J., Bernien, H., van Dam, S. B., Blok, M. S., Taminiau, T. H., … Hanson, R. (2014). Unconditional quantum teleportation between distant solid-state quantum bits. *Science*, *345*(6196), 532–535.

Pirandola, S., Bardhan, B. R., Gehring, T., Weedbrook, C., & Lloyd, S. (2018). Advances in photonic quantum sensing. *Nature Photonics*, *12*(12), 724–733.

Polino, E., Valeri, M., Spagnolo, N., & Sciarrino, F. (2020). Photonic quantum metrology. *AVS Quantum Science*, *2*(2), 024703.

Politi, A., Cryan, M. J., Rarity, J. G., Yu, S., & O'Brien, J. L. (2008). Silica-on-silicon waveguide quantum circuits. *Science*, *320*(5876), 646–649. https://doi.org/10.1126/science.1155441.

Prawer, S., & Greentree, A. D. (2008). Diamond for quantum computing. *Science*, *320*(5883), 1601–1602. https://doi.org/10.1126/science.1158340.

Preskill, J. (2019). Why I called it 'quantum supremacy'. *Quanta Magazine*, *2*(10), 2019.

Press, D., Götzinger, S., Reitzenstein, S., Hofmann, C., Löffler, A., Kamp, M., … Yamamoto, Y. (2007). Photon antibunching from a single quantum-dot-microcavity system in the strong coupling regime. *Physical Review Letters*, *98*(11), 117402.

Qiao, H., Kandel, Y. P., Manikandan, S. K., Jordan, A. N., Fallahi, S., Gardner, G. C., … Nichol, J. M. (2020). *Nature Communications*, *11*(1), 3022. https://doi.org/10.1038/s41467-020-16745-0.

Radu, V., Price, J. C., Levett, S. J., Narayanasamy, K. K., Bateman-Price, T. D., Wilson, P. B., & Mather, M. L. (2019). Dynamic quantum sensing of paramagnetic species using nitrogen-vacancy centers in diamond. *ACS Sensors*, *5*(3), 703–710.

Ralph, T. C., Langford, N. K., Bell, T. B., & White, A. G. (2002). Linear optical controlled-NOT gate in the coincidence basis. *Physical Review A*, *65*(6), 062324. https://doi.org/10.1103/PhysRevA.65.062324.

Ralph, T. C., & Pryde, G. J. (2010). Optical quantum computation. In *Progress in optics: Vol. 54* (pp. 209–269). Elsevier.

Ramalingam, G., Kathirgamanathan, P., Ravi, G., Elangovan, T., Arjunkumar, B., Manivannan, N., & Kasinathan, K. (2020). Quantum confinement effect of 2D nanomaterials. In *Quantum dots—Fundamental and applications*. IntechOpen.

Raussendorf, R., & Briegel, H. J. (2001). A one-way quantum computer. *Physical Review Letters, 86*(22), 5188–5191. https://doi.org/10.1103/PhysRevLett.86.5188.

Reck, M., Zeilinger, A., Bernstein, H. J., & Bertani, P. (1994). Experimental realization of any discrete unitary operator. *Physical Review Letters, 73*(1), 58–61. https://doi.org/10.1103/PhysRevLett.73.58.

Ren, J.-G., Xu, P., Yong, H.-L., Zhang, L., Liao, S.-K., Yin, J., … Pan, J.-W. (2017). *Nature, 549*(7670), 70–73. https://doi.org/10.1038/nature23675.

Riedrich-Moller, J., Arend, C., Pauly, C., Mucklich, F., Fischer, M., Gsell, S., … Becher, C. (2014). Deterministic coupling of a single silicon–vacancy color center to a photonic crystal cavity in diamond. *Nano Letters, 14*(9), 5281–5287.

Sala, E. M., Godsland, M., Trapalis, A., & Heffernan, J. (2021). Effect of cap thickness on InAs/InP quantum dots grown by droplet epitaxy in metal–organic vapor phase epitaxy. *Physica Status Solidi (RRL)—Rapid Research Letters, 15*(9), 2100283. https://doi.org/10.1002/pssr.202100283.

Samaner, Ç., Paçal, S., Mutlu, G., Uyanık, K., & Ateş, S. (2022). Free-space quantum key distribution with single photons from defects in hexagonal boron nitride. *arXiv preprint:2204.02830*.

Sanders, B. C. (2021). Quantum leap for quantum primacy. *Physics, 14*, 147.

Sangouard, N., Simon, C., Zhao, B., Chen, Y.-A., De Riedmatten, H., Pan, J.-W., & Gisin, N. (2008). Robust and efficient quantum repeaters with atomic ensembles and linear optics. *Physical Review A, 77*(6), 062301.

Scheidl, T., Ursin, R., Fedrizzi, A., Ramelow, S., Ma, X.-S., Herbst, T., … Zeilinger, A. (2009). *New Journal of Physics, 11*(8), 085002. https://doi.org/10.1088/1367-2630/11/8/085002.

Schimpf, C., Reindl, M., Huber, D., Lehner, B., Covre Da Silva, S. F., Manna, S., … Rastelli, A. (2021). Quantum cryptography with highly entangled photons from semiconductor quantum dots. *Science Advances, 7*(16), eabe8905.

Schrinner, P. P. J., Olthaus, J., Reiter, D. E., & Schuck, C. (2020). Integration of diamond-based quantum emitters with nanophotonic circuits. *Nano Letters, 20*(11), 8170–8177. https://doi.org/10.1021/acs.nanolett.0c03262. PMID: 33136413.

Schweickert, L., Jöns, K. D., Zeuner, K. D., Covre da Silva, S. F., Huang, H., Lettner, T., … Zwiller, V. (2018). On-demand generation of background-free single photons from a solid-state source. *Applied Physics Letters, 112*(9), 093106.

Shwetharani, R., Nayak, V., Jyothi, M. S., & Geetha Balakrishna, R. (2020). Review on recent advances of core-shell structured lead halide perovskites quantum dots. *Journal of Alloys and Compounds, 834*, 155246. https://doi.org/10.1016/j.jallcom.2020.155246.

Singh, A. (2021). Creation, Characterization, and Manipulation of Quantum Entanglement in a Photonic System (Ph.D. thesis). BangaloreRaman Research Institute.

Sinha, U. (2023). *Photon sources for quantum technologies, encyclopedia of materials: Electronics*. Elsevier. https://www.elsevier.com/books/encyclopedia-of-materials-electronics/abdul/978-0-12-819728-8.. ISBN 9780128197288.

Sinha, U., Couteau, C., Medendorp, Z., Söllner, I., Laflamme, R., Sorkin, R., & Weihs, G. (2009). Testing Born's rule in quantum mechanics with a triple slit experiment. In *Aip conference proceedings: Vol. 1101* (pp. 200–207).

Sinha, U., Sahoo, S. N., Singh, A., Joarder, K., Chatterjee, R., & Chakraborti, S. (2019). Single-photon sources. *Optics and Photonics News, 30*(9), 32–39. https://doi.org/10.1364/OPN.30.9.000032.

Smith, B. J., Mahou, P., Cohen, O., Lundeen, J. S., & Walmsley, I. A. (2009). Photon pair generation in birefringent optical fibers. *Optics Express*, *17*(26), 23589–23602. https://doi.org/10.1364/OE.17.023589.

Somaschi, N., Giesz, V., De Santis, L., Loredo, J. C., Almeida, M. P., Hornecker, G., ... Senellart, P. (2016). Near-optimal single-photon sources in the solid state. *Nature Photonics*, *10*(5), 340–345.

Sparavigna, A. C. (2022). Quantum computing logistics. *Available at SSRN 4249265*.

Sparrow, C., Paesani, S., Maraviglia, N., Santagati, R., Vigliar, C., Neville, A., & Laing, A. (2019). In *Quantum information and measurement (QIM) V: Quantum technologies* (p. p. S2C.2). Rome: OSA. https://doi.org/10.1364/QIM.2019.S2C.2.

Steiner, T. J., Castro, J. E., Chang, L., Dang, Q., Xie, W., Norman, J., ... Moody, G. (2021). Ultrabright Entangled-Photon-Pair generation from an AlGaAs-on-insulator microring resonator. *PRX Quantum*, *2*(1), 010337. https://doi.org/10.1103/PRXQuantum.2.010337.

Takemoto, K., Nambu, Y., Miyazawa, T., Sakuma, Y., Yamamoto, T., Yorozu, S., & Arakawa, Y. (2015). *Scientific Reports*, *5*(1), 14383. https://doi.org/10.1038/srep14383.

Takemoto, K., Nambu, Y., Miyazawa, T., Wakui, K., Hirose, S., Usuki, T., ... Arakawa, Y. (2010). *Applied Physics Express*, *3*(9), 092802. https://doi.org/10.1143/APEX.3.092802.

Tartakovskii, A. (2012). *Quantum dots: Optics, electron transport and future applications*. Cambridge University Press.

Tillmann, M., Dakić, B., Heilmann, R., Nolte, S., Szameit, A., & Walther, P. (2013). Experimental boson sampling. *Nature Photonics*, *7*(7), 540–544. https://doi.org/10.1038/nphoton.2013.102.

Toliver, P., Runser, R. J., Chapuran, T. E., Goodman, M. S., Jackel, J., McNown, S., & Dallman, N. (2007). Demonstration of 1550 nm QKD with ROADM-based DWDM networking and the impact of fiber FWM. In *Conference on lasers and electro-optics* (p. p. CThBB1). Optical Society of America.

Tran, T. T., Zachreson, C., Berhane, A. M., Bray, K., Sandstrom, R. G., Li, L. H., ... Toth, M. (2016). Quantum emission from defects in single-crystalline hexagonal boron nitride. *Physical Review Applied*, *5*(3), 034005.

Ursin, R., Jennewein, T., Aspelmeyer, M., Kaltenbaek, R., Lindenthal, M., Walther, P., & Zeilinger, A. (2004). *Nature*, *430*(7002), 849. https://doi.org/10.1038/430849a. 849.

Vagniluca, I., Da Lio, B., Rusca, D., Cozzolino, D., Ding, Y., Zbinden, H., ... Bacco, D. (2020). *Physical Review Applied*, *14*(1), 014051. https://doi.org/10.1103/PhysRevApplied.14.014051.

Wang, H., He, Y., Li, Y.-H., Su, Z.-E., Li, B., Huang, H.-L., ... Pan, J.-W. (2017). High-efficiency multiphoton boson sampling. *Nature Photonics*, *11*(6), 361–365. https://doi.org/10.1038/nphoton.2017.63.

Wang, H., Qin, J., Ding, X., Chen, M.-C., Chen, S., You, X., ... Pan, J.-W. (2019). Boson sampling with 20 input photons and a 60-mode interferometer in a 1 0 14-dimensional Hilbert space. *Physical Review Letters*, *123*(25), 250503.

Wang, L. J., Hong, C. K., & Friberg, S. R. (2001). Generation of correlated photons via four-wave mixing in optical fibres. *Journal of Optics B: Quantum and Semiclassical Optics*, *3*(5), 346.

Weerdt, F. D., Collins, A. T., Zugik, M., & Connor, A. (2005). Sub-threshold excitation of luminescence of defects in diamond. *Journal of Physics: Condensed Matter*, *17*(50), 8005. https://doi.org/10.1088/0953-8984/17/50/018.

Wen, K., Tamaki, K., & Yamamoto, Y. (2009). Unconditional security of single-photon differential phase shift quantum key distribution. *Physical Review Letters*, *103*(17), 170503.

Wikipedia, contributors. (2022). *F-center—Wikipedia, the free encyclopedia.*. https://en.wikipedia.org/w/index.php?title=F-center&oldid=1090784961.. Online; Accessed 3.11.22.

Wootters, W. K., & Zurek, W. H. (1982). A single quantum cannot be cloned. *Nature*, *299*(5886), 802–803. https://doi.org/10.1038/299802a0.

wu, W., Liu, W.-T., Chen, P.-X., & Li, C.-Z. (2010). Deterministic remote preparation of pure and mixed polarization states. *Physical Review A*, *81*, 042301. https://doi.org/10.1103/PhysRevA.81.042301.

Xia, Y., Lu, P.-M., Song, J., & Song, H.-S. (2010). Deterministic remote preparation of electrons states in coupled quantum dots by stimulated Raman adiabatic passage. *International Journal of Theoretical Physics*, *49*(9), 2045–2050.

Xiang, G.-Y., Li, J., Yu, B., & Guo, G.-C. (2005). Remote preparation of mixed states via noisy entanglement. *Physical Review A*, *72*(1), 012315.

Yan, Y., Zhai, D., Liu, Y., Gong, J., Chen, J., Zan, P., ... Chen, P. (2020). van der Waals heterojunction between a bottom-up grown doped graphene quantum dot and graphene for photoelectrochemical water splitting. *ACS Nano*, *14*(1), 1185–1195. https://doi.org/10.1021/acsnano.9b09554.

Yin, J., Cao, Y., Li, Y.-H., Ren, J.-G., Liao, S.-K., Zhang, L., ... Pan, J.-W. (2017). Satellite-to-ground entanglement-based quantum key distribution. *Physical Review Letters*, *119*(20), 200501. https://doi.org/10.1103/PhysRevLett.119.200501.

Zhao, J., Ma, C., Rüsing, M., & Mookherjea, S. (2020). High quality entangled photon pair generation in periodically poled thin-film lithium niobate waveguides. *Physical Review Letters*, *124*(16), 163603. https://doi.org/10.1103/PhysRevLett.124.163603.

Zhao, S., Lavie, J., Rondin, L., Orcin-Chaix, L., Diederichs, C., Roussignol, P., ... Lauret, J.-S. (2018). Single photon emission from graphene quantum dots at room temperature. *Nature Communications*, *9*(1), 3470.

Zhong, H.-S., Deng, Y.-H., Qin, J., Wang, H., Chen, M.-C., Peng, L.-C., ... Pan, J.-W. (2021). Phase-programmable gaussian boson sampling using stimulated squeezed light. *Physical Review Letters*, *127*(18), 180502. https://doi.org/10.1103/PhysRevLett.127.180502.

Zhong, H.-S., Wang, H., Deng, Y.-H., Chen, M.-C., Peng, L.-C., Luo, Y.-H., ... Pan, J.-W. (2020). *Science*, *370*(6523), 1460–1463. https://doi.org/10.1126/science.abe8770.